PARP-3 and APLF function together to accelerate nonhomologous end joining

Article (Accepted Version)

Highlights

- **PARP-3 activity is stimulated by DNA double-strand breaks**
- **PARP-3 accelerates DSB repair in concert with the ADP-ribose binding protein, APLF**
- **PARP-3 and APLF render chromatin 'permissible' for DNA ligation by XRCC4/DNA ligase IV**

PARP-3 and APLF Function Together to Accelerate Non-Homologous End Joining

Stuart L. Rulten[1], Anna E.O.Fisher[1], Isabelle Robert[2], Maria C. Zuma[1], Michele Rouleau[3], Limei Ju[1], Guy Poirier[3], Bernardo Reina-San-Martin[2], and Keith W. Caldecott[1]*

[1]Genome Damage and Stability Centre, University of Sussex, Falmer, Brighton, UK BN1 9RQ

[2]Institut de Génétique et de Biologie Moléculaire et Cellulaire (IGBMC), Department of Cancer Biology. Inserm U964 - CNRS UMR7104 - Université de Strasbourg, 67404 Illkirch CEDEX, France.

[3]Health and Environment Unit, Centre Hospitalier Universitaire de Québec, Laval Université Research Center, Québec, Québec, G1V 4G2, Canada

*To whom correspondence should be addressed: Tel 44 1273 877519; Fax 44 1272 678121; email k.w.caldecott@sussex.ac.uk

Running Title: PARP-3 and DNA double-strand break repair

Summary

PARP-3 is a member of the ADP-ribosyl transferase super-family of unknown function. We show that PARP-3 is stimulated by DNA double-strand breaks (DSBs) in vitro and functions in the same pathway as the poly (ADP-ribose)-binding protein APLF to accelerate chromosomal DNA double-strand break repair. We implicate PARP-3 in the accumulation of APLF at DSBs and demonstrate that APLF promotes the retention of XRCC4/DNA ligase IV complex in chromatin, suggesting that PARP-3 and APLF accelerate DNA ligation during non-homologous end-joining (NHEJ). Consistent with this, we show that class-switch recombination in Aplf$^{-/-}$ B cells is biased towards microhomology-mediated end-joining, a pathway that operates in the absence of XRCC4/DNA ligase IV, and that the requirement for PARP-3 and APLF for NHEJ is circumvented by overexpression of XRCC4/DNA ligase IV. These data identify molecular roles for PARP-3 and APLF and uncover a novel and unanticipated aspect of chromosomal DNA double-strand break repair reactions.

Highlights

- **PARP-3 activity is stimulated by DNA double-strand breaks**
- **PARP-3 accelerates DSB repair in concert with the ADP-ribose binding protein, APLF**
- **PARP-3 and APLF render chromatin 'permissible' for DNA ligation by XRCC4/DNA ligase IV**

Introduction

ADP-ribosyl transferases (ARTs) comprise a superfamily of enzymes that catalyse the post-translational modification of proteins and/or other molecules with ADP-ribose (Ame et al., 2004; Hottiger et al.; Otto et al., 2005). Currently, twenty-two members of the ART super-family have been identified with diverse roles in a variety of cellular processes including DNA repair, transcription, and cell death (Hottiger et al., 2010). Some ARTs modify proteins with chains of

poly (ADP-ribose) (pADPr) whereas others modify proteins with mono (ADP-ribose) (mADPr). The synthesis of pADPr by poly (ADP-ribose) polymerase-1 (PARP-1/ARTD1) is one of the earliest stages in the signalling and repair of DNA single-strand breaks (SSBs). Whilst SSBR still occurs in the absence of PARP-1 it does so at a reduced rate (Ding et al., 1992; Fisher et al., 2007; Le Page et al., 2003; Stevnsner et al., 1994; Trucco et al., 1998). The molecular role of pADPr synthesis at SSBs is unclear but most likely includes the modification of chromatin structure (Poirier et al., 1982) and promoting the localised accumulation of DNA repair proteins that bind directly to pADPr (El-Khamisy et al., 2003; Okano et al., 2003; Rulten et al., 2008).

pADPr synthesis by PARP-1 has also been implicated in the cellular response to DNA double-strand breaks (DSBs)(Audebert et al., 2004; Benjamin and Gill, 1980; Boulton et al., 1999; Morrison et al., 1997). The role of PARP-1 at DSBs is not known but may include repressing core non-homologous end-joining (NHEJ) and/or promoting homologous recombination at damaged replication forks (Bryant et al., 2009; Hochegger et al., 2006; Sugimura et al., 2008; Yang et al., 2004). Recently, PARP-2/ARTD2 has also been implicated in promoting homologous recombination, perhaps explaining the embryonic lethality observed in mice lacking both PARP-1 and PARP-2 (Bryant et al., 2009). PARP-1 may also promote a 'back-up' pathway of non-homologous end joining (NHEJ) known as alternative NHEJ, though the nature of this role is unclear (Audebert et al., 2004; Boulton et al., 1999; Brown et al., 2002; Robert et al., 2009; Wang et al., 2006). Of the remaining twenty human ARTs currently identified only PARP-3/ARTD3, PARP-4/ARTD4, and PARP-5/ARTD5 are likely to possess poly (ADP-ribose) polymerase activity (Hottiger et al., 2010). Whereas PARP-4 (vault PARP) and PARP-5 (tankyrase 1) function within ribonucleoprotein complexes and at telomeres, respectively, the role of PARP-3 is unknown (Kickhoefer et al., 1999; Smith et al., 1998). Whilst PARP-3 has been reported to co-immunoprecipitate with polycomb protein complexes and a variety DNA repair proteins, it has not been reported to be activated by DNA, suggesting that this enzyme is not a sensor molecule for DNA strand breaks (Loseva et al., 2010; Rouleau et al., 2007).

PARP-1 inhibitors have received much attention recently because of their potential application as monotherapeutic anti-cancer agents in individuals with hereditary mutations in the tumour suppressor genes BRCA1 or BRCA2 (Bryant et al., 2005; Farmer et al., 2005). However, such agents not only inhibit PARP-1 and PARP-2 but can also inhibit PARP-3 (Loseva et al.,

2010). An understanding of PARP-3 function is thus important not only from a basic cell biology perspective but also from a clinical perspective. Here, we have addressed the role of PARP-3 in human cells. We demonstrate that PARP-3 is activated by DSBs in vitro and accelerates DSB repair by facilitating DNA ligation. This work identifies a molecular role for PARP-3 and reveals a novel aspect of non-homologous end-joining.

Results

PARP-3 Accelerates DSBR in Human Cells Following γ-Irradiation.

To address the role of poly (ADP-ribose) (pADPr) during DSBR we first compared rates of γH2AX induction and removal following γ-irradiation in A549 cells pre-treated with the PARP inhibitor, KU-58948. Although sites of γH2AX can arise by different mechanisms, the number of γH2AX foci detected in a cell following γ-irradiation closely reflects the number of chromosomal DSBs (Lobrich et al., 2010; Rogakou et al., 1999; Rogakou et al., 1998). Notably, pre-treatment with 500 nM KU-58948, a concentration of this PARP inhibitor sufficient to inhibit PARP-1, PARP-2, and PARP-3 in vitro (Lehtio et al., 2009; Loseva et al., 2010), significantly delayed the rate at which γH2AX foci declined in A549 cells at early times (<2 hr) following γ-irradiation (Fig.1A & Supplementary Fig.1B). We noted, however, that the level of γH2AX foci remaining in A549 cells treated with PARP inhibitor was similar at later times after γ-irradiation, suggesting that PARP inhibition delays but does not prevent DSBR (data not shown). To identify which PARP enzyme affected the level of γH2AX foci following γ-irradiation we employed A549 cells in which PARP-1, PARP-2, or PARP-3 was depleted by shRNA. The rate of decline of γH2AX in PARP-1 or PARP-2-depleted A549 cells was not significantly different than in mock-depleted cells (Fig.1B & 1C). In contrast, depletion (by ~80%) of PARP-3 delayed the decline of γH2AX to a similar extent as PARP inhibition with KU-58948 (Fig.1A & 1C). Neither PARP-1 or PARP-2 protein levels (Fig.1F) or global levels of pADPr synthesis (Supplementary Fig.1D) were altered in PARP-3-depeleted cells, suggesting that PARP-3 depletion does not slow DSBR by affecting these enzymes. Notably, KU-58948 failed to delay the decline of γH2AX in cells depleted of PARP-3, confirming that PARP inhibition and PARP-3 depletion inhibit the same DSBR pathway (Fig.1A). Importantly, the defect in γH2AX decline conferred by PARP-3 depletion was complemented by expression of

wild-type shRNA-resistant (i.e. targeting-resistant) PARP-3 cDNA (PARP-3^{TR}), but not by targeting-resistant PARP-3 harbouring a mutated catalytic domain (PARP-3^{TR} CM)(Fig.1D & 1E). We conclude that PARP-3 activity accelerates the rate of DSBR in A549 cells following γ-irradiation.

PARP-3 Activity is Stimulated by DSBs, in vitro.

Given the apparent impact of PARP-3 on the rate of DSBR we examined whether PARP-3 activity was stimulated by DNA, in vitro. Recombinant human PARP-3 (Alexis) (Fig.2A, left) was incubated with [^{32}P]-NAD^+ in the absence or presence of different DNA structures and radiolabelled ribosylated protein products detected by SDS-PAGE and autoradiography. In the absence of DNA, we observed relatively little ribosylated protein product (Fig.2B, lane 1). However, in the presence of sonicated salmon sperm ('SS') DNA we detected a single ribosylated polypeptide that co-migrated with PARP-3, suggesting that PARP-3 autoribosylation was stimulated by DNA (Fig.2B, lane 2). To examine whether PARP-3 is activated by DSBs, we next compared the activity of this enzyme in reactions containing a series of defined DNA substrates. Whereas single-stranded oligonucleotides had little or no effect on PARP-3 activity, equivalent (equimolar) amounts of double-stranded oligonucleotides stimulated PARP-3 automodification (Fig.2B, lanes 3-9). We noted in these experiments that oligonucleotide duplexes with 5'- or 3'-overhangs stimulated PARP-3 to a greater extent than did blunt-ended duplexes (Fig. 2B, lanes 7-9). To confirm that PARP-3 is stimulated by DSBs we compared the activation of this enzyme by limiting amounts of uncut supercoiled pEGFP-C2 plasmid and by pEGFP-C2 cut once or twenty-four times per plasmid molecule (Fig.2C, top). Strikingly, whereas uncut supercoiled plasmid (SC) failed to stimulate PARP-3 autoribosylation, plasmid cut once or twenty-four times stimulated this enzyme ~2-10 fold (Fig.2C, top & middle, lanes 2-7). Once again, we noted that DNA harbouring DSBs with single-stranded overhangs, particularly 5'-overhangs, stimulated PARP-3 to a greater extent than DSBs with blunt ends.

Whilst we failed to detect evidence of other, contaminating, PARP enzymes (as measured by autoribosylation activity) in the PARP-3 preparation employed above (Supplementary Fig. 2), we repeated our experiments with three additional independent sources of PARP-3. First, we employed recombinant human histidine-tagged PARP-3 (His-PARP-3) that we expressed in

insect cells and purified by metal-chelate chromatography (Fig.2A, right). Remarkably, the results obtained with His-PARP-3 were almost identical to those observed with untagged PARP-3, with ribosylation of His-PARP-3 stimulated by cut plasmid (Fig. 2C, bottom). Secondly, we employed GST-tagged PARP-3 (GST-PARP-3) purified from insect cells by glutathione affinity chromatography (Abcam), which similarly was stimulated by DSBs (Fig.2D). Finally, we employed recombinant human His-PARP-3 that we expressed in E.coli and purified by metal-chelate chromatography, and in parallel a derivative of His-PARP-3 harbouring a mutated catalytic domain (denoted His-PARP-3^{CM}). Notably, autoribosylation of human His-PARP-3 purified from E.coli was also stimulated by DSB substrate, whereas His-PARP-3^{CM} lacked detectable activity (Fig.2E). Together, these data demonstrate that PARP-3 is stimulated by DSBs and suggest that this enzyme is a novel DSB 'sensor'.

PARP-3 Accelerates Chromosomal DSBR Together with Aprataxin-and-PNK-like Factor (APLF)

What role might PARP-3 play during DSBR? At chromosomal SSBs PARP-1 promotes the accumulation of Aprataxin-and-PNK-Like Factor (APLF), a protein that binds tightly to poly (ADP-ribose) via a C-terminal tandem zinc finger domain (PBZ domain) (Ahel et al., 2008; Bekker-Jensen et al., 2007; Iles et al., 2007; Kanno et al., 2007; Rulten et al., 2008). We thus wondered whether the role of PARP-3 at chromosomal DSBs might be mediated via APLF. Consistent with this idea, recombinant YFP-APLF protein accumulated at sites of γH2AX following γ-irradiation, supporting the idea that this protein accumulates at chromosomal DSBs (Fig.3A). Moreover, pre-incubation with 500nM PARP inhibitor (KU-58948) greatly reduced or abolished the focal accumulation of YFP-APLF, as did mutation of the ADP-ribose-binding PBZ domain (Fig. 3B). We have shown previously that APLF is likely targeted to SSBs by binding to auto-ribosylated PARP-1 or to histone H1 that has been trans-ribosylated by PARP-1 (Rulten et al., 2008). To examine whether PARP-3 might play a similar role at DSBs, we determined whether APLF can bind to slot-blotted human His-PARP-3 (purified from insect cells) and/or histone H1 following their auto- or trans-ribosylation. Ribosylation of histone H1.2 by His-PARP-3 was at least as efficient as His-PARP-3 autoribosylation, in reactions containing equivalent amounts of the two proteins, suggesting that histone H1 is an efficient substrate for

PARP-3 (Fig.3C, top left). Interestingly, the ADP-ribose product of histone H1.2 ribosylation was primarily mono ADP-ribose (mADPr), with lower amounts of ADP-ribose chains of up to ~15 units also present (Fig.3C, right). This is consistent with the prediction that glutamate residue E514 of PARP-3 catalyses polyribosylation of its target proteins (Hottiger et al., 2010; Kleine et al., 2008). Importantly, APLF bound both His-PARP-3 and histone H1 in a manner that was stimulated by or dependent on their ribosylation, respectively (Fig.3C, lower left).

Taken together, the data described above suggest that PARP-3 accelerates DSBR by targeting APLF to chromosomal DSBs, most likely via binding of the latter to ribosylated histone H1. Consistent with this idea, we have reported previously that γH2AX foci also decline at a reduced rate in APLF-depleted A549 cells at early times following γ-irradiation (Iles et al., 2007). This is not an indirect impact of reduced rates of single-strand break repair in APLF-depleted cells, due to increased conversion of SSBs into DSBs during S phase, because the rate of γH2AX decline was also delayed in APLF-depleted cells following γ-irradiation in G1 and G2 (Supplementary Fig.1C). To address the relationship between APLF and PARP-3 during DSBR, directly, we compared the rate at which γH2AX foci declined in A549 cells depleted of either protein with that in cells depleted of both. Depletion of both APLF and PARP-3 did not slow the decline of γH2AX foci following γ-irradiation much more than did depletion of PARP-3 or APLF alone, suggesting that these two proteins function in the same pathway during DSBR (Fig.4A). Consistent with this, as observed in PARP-3-depleted cells (see Fig.1C), 500nM PARP inhibitor (KU-58948) failed to further reduce the rate at which γH2AX foci declined in APLF-depleted A549 cells (Fig.4B). This contrasted with PARP-1-depleted cells, in which APLF depletion and/or KU-58948 treatment slowed the rate of γH2AX decline to a similar extent (Fig.4C). We next examined whether the requirement for APLF during DSBR required the C-terminal PBZ domain, as predicted if binding to ADP-ribose at chromosomal DSBs is important for APLF to accelerate DSBR. We thus created targeting-resistant derivatives of wild-type APLF ($APLF^{TR}$) and APLF harbouring a mutated PBZ domain (APLF-$Zfm1^{TR}$) and compared these proteins for ability to restore normal rates of γH2AX decline in APLF-depleted A549 cells. Indeed, whereas stable expression of $APLF^{TR}$ restored the decline of γH2AX foci to normal, stable expression of APLF-$Zfm1^{TR}$ that cannot bind pADPr did not (Fig.5A). Together, these data suggest that PARP-3 accelerates DSBR in A549 cells via APLF, most likely by promoting recruitment or retention of the latter protein at chromosomal DSBs. We reasoned that if this was

true then it might be possible to bypass the requirement for PARP-3 by transient over-expression of APLF, thereby increasing the localized concentration of the latter. Indeed, whereas over-expression of APLF failed to alter the rate of γH2AX decline in wild-type A549 cells it restored this rate to normal in PARP-3-depleted A549 cells (Fig.5B). Together, these data suggest that PARP-3 accelerates the early rate of DSBR in A549 cells via APLF.

PARP-3 and APLF Promote DSBR by Accelerating DNA Ligation

APLF directly interacts with XRCC1 and XRCC4, both of which are components of the cellular DNA ligation machinery (Bekker-Jensen et al., 2007; Iles et al., 2007; Kanno et al., 2007; Macrae et al., 2008). Whereas XRCC1 interacts with DNA ligase III (Lig3) and functions during single-strand break repair (Caldecott et al., 1994; Caldecott et al., 1995), XRCC4 interacts with DNA ligase IV (Lig4) and functions during the non-homologous end joining (NHEJ) pathway of DSBR (Critchlow et al., 1997; Grawunder et al., 1997). We thus wondered whether the role of APLF at chromosomal DSBs might be to promote the recruitment and/or retention of XRCC4/Lig4 heterodimer. To examine this, we measured the accumulation of GFP-XRCC4 at sites of UVA laser-induced DNA damage in transiently-transfected cells, an approach that has been employed previously to measure recruitment and retention of NHEJ proteins at sites of DNA damage (Yano and Chen, 2008; Yano et al., 2008). Whilst GFP-XRCC4 accumulated rapidly at sites of laser damage in both wild-type and APLF-depleted A549 cells, reaching a steady-state level within 2 min, it did so more slowly and less extensively in APLF-depleted cells (Fig.6A). Importantly, the rate and extent of accumulation of GFP-XRCC4 at sites of UVA laser-induced DNA damage was restored to normal by stable expression of targeting-resistant APLF^{TR} (Fig.6B). In contrast, stable expression of targeting-resistant APLF Zfm1^{TR}, in which the first zinc finger of PBZ domain is mutated, exhibited partial restoration of GFP-XRCC4 accumulation (Fig.6B). The intermediate impact of this mutation may reflect weak but residual ADP-ribose binding activity provided by the ZnF2 domain, in combination with high over-expression of GFP-XRCC4, or possibly a level of GFP-XRCC4 accumulation via the PBZ-independent interactions of APLF with XRCC4 and Ku80 (Iles et al., 2007; Kanno et al., 2007; Macrae et al., 2008).

To examine whether APLF similarly promotes the recruitment and/or stability of endogenous XRCC4 in chromatin we conducted sub-cellular fractionation experiments. Indeed, levels of endogenous XRCC4 were markedly less in the chromatin-containing fraction of APLF-depleted A549 cells than in that of mock-depleted cells, following γ-irradiation (Fig.6C compare lanes 4-6 with lanes 8-10). Notably, levels of XRCC4 were also reduced in the chromatin-containing fraction of APLF-depleted A549 cells before γ-irradiation, suggesting that APLF also promotes the stability of XRCC4 in chromatin at endogenous levels of DNA damage (Fig.6C, compare lanes 3 & 7). These results did not reflect a global reduction in chromatin-associated protein levels in APLF-depleted cells, because the level of histone protein in the chromatin-containing fractions was unaffected (Fig.6C, bottom panel). Together, these data suggest that APLF promotes the stability or retention of XRCC4 in chromatin.

Since XRCC4 is a cofactor for Lig4, we reasoned that the primary role of APLF may be to promote DNA ligation at chromosomal DSBs. If true, we considered it possible that co-overexpression of XRCC4 and Lig4 might circumvent the requirement for APLF for normal rates of DSBR following γ-irradiation. Indeed, the rate at which γH2AX foci declined in APLF-depleted cells following γ-irradiation was restored to normal by overexpression of both XRCC4 and Lig4, but not by overexpression of XRCC4 alone (Fig.7A). Since APLF functions epistatically with PARP-3 during DSBR we examined whether over-expression of XRCC4 and Lig4 similarly restored normal rates of γH2AX decline in PARP-3–depleted cells. Indeed, the rate at which γH2AX foci declined in PARP-3-depleted cells following γ-irradiation was restored to normal by overexpression of both XRCC4 and Lig4 (Fig.7B). We thus conclude that the primary role of APLF during NHEJ in human cells is to maintain high localised concentrations of XRCC4/Lig4 in damaged chromatin, thereby promoting rapid and efficient DNA ligation.

Increased microhomology at class switch recombination junctions in Aplf$^{-/-}$ B cells.

Given that PARP-3 and APLF are not essential for NHEJ but rather accelerate the rate of this process, we wondered whether loss of this axis might impact on NHEJ-dependent events, in vivo. To address this we obtained Aplf$^{+/-}$ mice from the International Gene Trap Consortium and from these derived homozygous Aplf$^{-/-}$ mice (Supplementary Fig.3). Importantly, similar to APLF-depleted human cells, γH2AX foci declined at a reduced rate in Aplf$^{-/-}$ mouse embryonic

fibroblasts following γ-irradiation, confirming the results of our RNA interference experiments (Fig.7C). We next exploited the observation that class switch recombination (CSR) during antibody diversification is reduced in mouse B lymphocytes in which XRCC4 is deleted, and that the residual CSR in such cells is biased towards 'alternative' NHEJ events that generate increased levels of microhomology at the CSR junctions (Soulas-Sprauel et al., 2007; Yan et al., 2007). We therefore examined whether loss of APLF similarly impacted on CSR in B lymphocytes isolated from $Aplf^{-/-}$ mouse spleens. The proliferation rate and overall efficiency of CSR appeared normal in $Aplf^{-/-}$ B cells (Supplementary Fig.4). However, sequencing of Sμ/Sγ3 CSR junctions revealed a significant shift towards microhomology-mediated NHEJ (Fig.7D), with a mean overlap of 1.9 bp and 2.7 bp in $Aplf^{+/+}$ and $Aplf^{-/-}$ cells, respectively. In addition, whereas the proportion of $Aplf^{+/+}$ junctions displaying two or more base pairs of microhomology was 35%, this was increased to 63% in $Aplf^{-/-}$ sequences (Fig. 7D and Supplementary Fig. 5). We conclude that the impact of Aplf deletion on the rate of 'classical' NHEJ in splenic B cells is sufficient to bias CSR towards alternative microhomology-mediated events.

Discussion

We show here that PARP-3 accelerates the rate at which γH2AX foci decline following γ-irradiation, and preliminary experiments suggest that PARP-3 may also accelerate γH2AX decline following treatment with other genotoxins (Supplementary Figure 6). Although sites of γH2AX are an indirect measure of chromosomal DSBs and can arise independently of these lesions, they provide a reliable and sensitive method for measuring DSBR rates following γ-irradiation (Lobrich et al., 2010). Indeed, following γ-irradiation, the number of γH2AX foci detected in a cell closely reflects the number of chromosomal DSBs. The epistatic relationship with APLF further implicates PARP-3 in DSBR, since APLF is a bona fide DSBR protein that interacts directly with the core non homologous end joining (NHEJ) factors Ku80 and XRCC4 (Iles et al., 2007; Kanno et al., 2007; Macrae et al., 2008). It is also noteworthy that $Aplf^{-/-}$ B lymphocytes exhibited increased levels of microhomology at class-switch recombination junctions, a hallmark feature of cells in which 'classical' NHEJ is reduced (Soulas-Sprauel et al., 2007; Yan et al., 2007). This is in contrast to $Parp\text{-}1^{-/-}$ B cells, which exhibit decreased levels of microhomology at class-switch recombination junctions, consistent with the reported role of this

protein in 'alternative' NHEJ (Audebert et al., 2004; Brown et al., 2002; Robert et al., 2009; Wang et al., 2006). The CSR phenotype in $Aplf^{-/-}$ B cells is milder than that observed in B cells lacking core NHEJ factors, most likely because APLF accelerates NHEJ rather than being essential for this process. A role for PARP-3 in DSBR was also suggested by the ability of XRCC4/Lig4 overexpression to complement the slow rate of γH2AX decline in PARP-3-depleted cells, suggesting that this slow rate resulted from inefficient DNA ligation. Finally, PARP-3 activity was stimulated by DSBs in vitro. We note that this finding disagrees with a previous report, in which it was concluded that PARP-3 is not activated by DNA (Loseva et al., 2010). This may reflect the presence of DNA fragments in the PARP-3 preparations employed by Loseva et al, since the inclusion of sonication during the purification procedure can result in partial pre-activation of recombinant PARP-3 (unpublished observations).

What is the role of PARP-3 during NHEJ? One role of PARP-1 is to target APLF to chromosomal SSBs via an interaction between the poly (ADP-ribose)-binding (PBZ) domain in APLF and one or more poly (ADP-ribosylated) chromatin proteins (Ahel et al., 2008; Bekker-Jensen et al., 2007; Kanno et al., 2007; Rulten et al., 2008). It thus seems plausible that PARP-3 targets APLF to chromosomal DSBs in a similar way. This is supported by several observations. First, over-expression of APLF restored normal rates of γH2AX decline in PARP-3-depleted cells, suggesting that the role of PARP-3 in accelerating NHEJ was circumvented by increasing the cellular concentration of APLF. Second, the PARP-mediated accumulation of APLF at DSBs required the ADP-ribose binding domain of APLF, consistent with this accumulation involving direct interaction of APLF with ADP-ribose. Given that PARP-3 accelerates 'classical' NHEJ it seems likely that this enzyme will function cooperatively with DNA-PK. PARP-3 may bind to a DSB after DNA-PK has been released from the break and Ku has translocated away from the DNA termini. This would allow access at the break both to any DNA end processing factors required to repair the damaged termini [reviewed recently in (Mahaney et al., 2009)] and to PARP-3 in preparation for APLF recruitment and DNA ligation.

Our data suggest that PARP-3 accelerates NHEJ via APLF, but what is the role of APLF? Based on our data we propose that APLF renders chromatin in the vicinity of a DSB more 'permissive' for DNA ligation, at least in part by promoting the retention of XRCC4-Lig4 heterodimer at chromosomal DSBs. This idea is supported not only by the reduced accumulation of GFP-XRCC4 at localised DNA damage induced by UVA laser in APLF-depleted A549 cells,

but also by the reduced level of endogenous XRCC4 in chromatin-containing fractions of these cells. Moreover, co-overexpression of XRCC4 and Lig4, but not XRCC4 alone, circumvented the requirement for APLF for normal rates of NHEJ, strongly suggesting that the reduced rate of DSBR in APLF-depleted cells results from sub-optimal DNA ligase activity. It is currently unclear how XRCC4/Lig4 retention is stabilised by APLF, but one possibility is that APLF anchors XRCC4 in chromatin directly. This may be achieved via the established interaction between APLF and XRCC4 (Iles et al., 2007) and via an interaction between the PBZ domain of APLF and ribosylated histone H1. Intriguingly, overexpression of APLF rescued the rate of DSBR even in PARP-3-depleted cells. Whilst the residual PARP-3 in these cells might be sufficient to support DSBR in the presence of overexpressed APLF, this observation raises the possibility that APLF might render chromatin more permissive for ligation even in the absence of ADP ribosylation. If so, APLF may thus also modify chromatin structure at DSBs, directly. In addition to XRCC4, APLF also interacts with Ku80, and both APLF and Ku have been suggested to process damage DNA termini (Kanno et al., 2007; Roberts et al., 2010). Whilst we cannot rule out a role for APLF in DNA end processing, the restoration of normal rates of γ-H2AX decline in APLF-depleted cells by XRCC4/Lig4 over-expression suggests that the primary role of APLF in accelerating DSBR is to promote DNA ligation. A model for the role of PARP-3 and APLF is presented in Fig.7E.

In summary, we report here that PARP-3 and APLF promote the retention of XRCC4/DNA ligase IV in chromatin and promote non-homologous end joining. These data identify a molecular role for PARP-3 and APLF and uncover a novel and unanticipated aspect of chromosomal DNA double-strand break repair reactions in human cells.

Acknowledgements

This work was funded by grants to KC from the BBSRC (BB/F013930/1), MRC (G0600776), and CR-UK (C6563/A101192). The authors wish to thank Liandi Guo for technical assistance.

Experimental Procedures

Plasmids, Recombinant Proteins, Aplf$^{-/-}$ mice, and Biochemical Experiments

The description of plasmids, recombinant proteins, biochemical experiments, and Aplf$^{-/-}$ mice are provided in Supplemental Experimental Procedures. Fractionation experiments were carried out essentially as described (Drouet et al., 2005), and are described in detail in Supplementary Experimental Procedures.

RNA interference

Details of RNA interference experiments are in Supplementary Experimental Procedures. In brief, cells were transiently-co-transfected with pCD2E (encoding G418r selectable marker) and one or more appropriate pSUPER shRNA constructs and transfected cell-pools selected in G418 medium for 5 days. For complementation experiments, transiently-depleted or stably-depleted cells were transfected with expression construct encoding the relevant targeting-resistant (shRNA-resistant) ORF or encoding GFP-XRCC4 and/or DNA ligase IV.

Immunofluorescence

Analysis DSBR by γH2AX foci immunofluorescence is described in detail in Supplementary Experimental Procedures. In brief, A549 cells on coverslips were mock-treated or irradiated (2Gy) and incubated at 37°C for the times stated to allow repair. Cells were then immunstained for γH2AX foci and γH2AX foci counted microscopically.

Laser microirradiation

Laser experiments are described in detail in Supplementary Experimental Procedures. In brief, A549 cells were seeded onto glass-bottom dishes and transfected with pEGFP-XRCC4. GFP-positive cells were then irradiated with a 351-nm UVA laser and images subsequently captured at 30 s intervals.

Figure Legends

Figure 1: PARP-3 depletion delays the rate of DSBR in human cells following γ-irradiation.

[A] Mock-depleted (A549) or transiently-PARP-3-depleted (A549-PARP3^{KD}) A549 cells were pre-treated where indicated with 500 nM PARP inhibitor KU-58948 (+ Pi) and either mock-irradiated ('Unt') or γ-irradiated (2 Gy). Cells were fixed at the times indicated for analysis by γH2AX immunofluorescence. The average number of γH2AX foci per cell is shown. "KD" denotes shRNA-mediated knock-down. Data are the mean of at least three independent experiments (+/- SEM). p values in parentheses reflect the statistical comparison (2-way ANOVA) between the wild-type (A549) data set and the indicated data set, except for those indicated by a right brace, which reflect the statistical comparison between the indicated data sets. "NS" denotes not significant (p value >0.05).

[B] A549 cells mock-depleted (A549) or transiently-depleted of PARP-1 (A549-PARP1^{KD}) were mock-irradiated ('Unt') or γ-irradiated (2 Gy) and analysed as described above.

[C] Mock-depleted (A549) or transient PARP-2-depleted (A549-PARP2^{KD}) or PARP-3-depleted (A549-PARP3^{KD}) A549 cells were mock-irradiated ('Unt') or γ-irradiated (2 Gy) and analysed as described above.

[D] Mock-depleted (A549) or transient PARP-3-depleted (A549-PARP3^{KD}) A549 cells were co-transfected with empty vector (+Vector) or with an expression construct encoding targeting-resistant PARP-3 (+PARP3^{TR}). Mock-irradiated ('Unt') or γ-irradiated (2 Gy) cells were analysed as described above.

[E] Mock-depleted (A549) or transiently-PARP-3-depleted (A549-PARP3^{KD}) A549 cells were co-transfected with either empty vector (+Vector) or with an expression construct encoding either targeting-resistant wild-type PARP-3 (+PARP3^{TR}) or a catalytic-mutant of targeting-resistant PARP-3 (+PARP3^{TR} CM). Mock-irradiated ('Unt') or γ-irradiated (2 Gy) cells were analysed as described above. p values are from a 2-tailed paired T-test.

[F] Representative western blots showing levels of the indicated proteins in the cells employed in panels A-E, above. Top, levels of PARP-3 ('P3'), PARP-1 (P1), PARP-2 (P2), and tubulin ('tub' in the PARP-3-depleted cells (A549-PARP3^{KD}). Asterisk denotes a non-specific band. Bottom Left, PARP-1, PARP-2 and actin levels in mock-depleted A549 cells (A549), PARP-1-depleted cells (A549-PARP1^{KD}), and PARP-2-depleted cells (A549-PARP2^{KD}). Bottom right, levels of PARP-3 ('P3', arrow) and Tubulin ('tub') in PARP-3-deleted cells (PARP3^{KD}) transfected with either empty vector ('Vect'), expression construct encoding targeting-resistant wild-type PARP-3

(+PARP3^{TR} ; 'P3'), or catalytically-mutated targeting-resistant PARP-3 (+PARP3^{TR} CM; 'P3^{CM}').

Figure 2: PARP-3 activity is stimulated by DSBs in vitro.

[A] Coomassie blue-stained SDS-PAGE gels containing 2.5μg of PARP-3 protein (Alexis, left) or His-PARP-3 (right) employed in these experiments, along with the relevant molecular mass marker (M).

[B] Recombinant human PARP-3 (180nM; Alexis) was incubated with 0.5μM ^{32}P-NAD$^+$/2μM NAD$^+$ in the absence of DNA (-) or in the presence of either 50 ng sonicated salmon sperm DNA (SS) or 2μM of the indicated 30-bp or 43-bp single- or double-stranded oligonucleotide substrates. The single-stranded oligonucleotides were 43F (lane 3), 43R (lane 4), 30F (lane 5), and 30R (lane 6). The double-stranded oligonucleotides were 30F+43R (lane 7; duplex with 13-bp 5'-overhang), 43F+30R (lane 8; duplex with 13-bp 3'-overhang), and 43F+43R (lane 9; duplex with blunt-ends). Reaction products were separated on acid SDS-PAGE gels and analysed by phosphorimaging.

[C] Top, pEGFP-C2 plasmid that was either supercoiled (lane 2), linearized with NheI (lane 3; 4-bp 5'-overhang), KpnI (lane 3; 4-bp 3'-overhang), or Eco47III (lane 5; blunt end), or cut at 24 sites per molecule with either Sau3AI (lane 6; 4-bp 5'-overhang) or HhaI (lane 7; 2-bp 3'-overhang), was separated and detected with ethidium bromide/UV following agarose gel electrophoresis. **Middle**, Recombinant human PARP-3 (125nM; Alexis) was incubated with 0.25μM ^{32}P-NAD$^+$/1μM NAD$^+$ as indicated in the absence of DNA or in the presence of 100ng of the indicated pEGFP-C2 plasmid described above. Values below the gel are fold-increases in ribosylated PARP-3 quantified by densitometry and normalised to the band intensity in the absence of DNA (set at 1), from three independent experiments (+/- SEM in parentheses). **Bottom,** Recombinant human His-PARP-3 (250nM) was incubated with 0.25μM ^{32}P-NAD$^+$/1μM NAD$^+$ and 100ng of the indicated pEGFP-C2 plasmid as described above. Note that in these experiments the concentration of plasmid DSB termini was 0nM (supercoiled), 2.6nM (linear), and 61.4nM (cut x 24).

[D] Left, recombinant human His-PARP-3 (His-P3; 1μM) or GST-PARP-3 (GST-P3; Abcam; 200nM) was incubated with 0.5μM ^{32}P-NAD$^+$/2μM NAD$^+$ as indicated in the absence of 400ng

(0.67μM) of an oligonucleotide duplex (30F+43R) with a 13-bp 5'-overhang. Reaction products were separated on acid SDS-PAGE gels, fixed, dried, and detected on a phosphorimager. Right, 2.5μg each of His-PARP-3 (His-P3) or GST-PARP-3 (GST-P3) was fractionated by SDS-PAGE along with molecular mass markers (M) and stained with coomassie blue.
[E] Recombinant wild-type (His-P3) or catalytic mutant (His-$P3^{CM}$) human His-PARP3 (250nM) purified from E.Coli was incubated with 0.5μM ^{32}P-NAD^+/80μM NAD^+ in the absence or presence of oligonucleotide duplex DSB substrate (400nM) as indicated. Reaction products were separated on an SDS-PAGE gel, stained with coomassie blue (top), and analysed by phosphorimaging (bottom). The position of His-PARP-3 and His-PARP-3 is shown (P3/ $P3^{CM}$).

Figure 3: APLF binds PARP-3-ribosylated substrates and accumulates at DSBs in a PARP-activity dependent manner

[A] A549 cells transiently-transfected with pEYFP-APLF (green) were mock-irradiated (-IR, top) or γ-irradiated (2Gy) (+IR, bottom) and 30 min later fixed and immunostained with anti-γH2AX antibody (red). DNA was counterstained with DAPI (blue).

[B] A549 cells transiently-transfected with expression construct encoding either pEYFP-APLF or pEYFP- $APLF^{Zfm1}$ (harbouring a mutated ADP-ribose-binding PBZ domain) were analysed as described above and the fraction of transfected (green) cells with detectable YFP foci was quantified. Where indicated, cells were pre-treated with the PARP inhibitor KU-58948 (500nM) for 30 min prior to γ-irradiation (+Pi).

[C] Top Left, His-PARP-3 (purified from insect cells) and histone H1 (1.9μM each) were incubated separately or together in the presence of 0.25μM ^{32}P-NAD^+ in ribosylation buffer containing 50ng DNA for 10 min at 30^{o}C. Reactions products were separated by SDS-PAGE and analysed by phosphorimager. A coomassie stained gel of the recombinant His-PARP-3 and histone H1.2 employed above is shown. Bottom Left, 1μg of either histone H1.2 (H1.2) or 0.5μg His-PARP-3 (His-P3) was slot blotted onto nitrocellulose and either stained with amido black as a loading control (right panel) or incubated with His-PARP-3 (3μM) in the presence or absence of 150μM NAD^+ (+/-NAD) as indicated (left panel). The filters from mock-ribosylation (-NAD) and ribosylation (+NAD) reactions were then incubated or not with APLF probe (10nM), as

indicated. After extensive washes bound APLF was detected with anti-APLF antibody. Right, multiwell dishes coated with histone H1.2 were incubated with 1.5μM BSA or His-PARP-3 in the presence of 2μM ^{32}P-NAD^{+} and 600ng (24ng/μl) Sau3AI-cut pEGFP-C2 plasmid and after extensive washing reaction products were released from the multiwell dishes by trypsin digestion, fractionated on a polyacrylamide sequencing gel, and detected by phosphorimager. The position of mADPR (n) and pADPR of two or more units (2n, 3n, 4n etc) are indicated.

Figure 4: PARP-3 and APLF function cooperatively during DSBR

[A] A549 cells mock-depleted (A549) or transiently-depleted of either PARP-3 (A549-PARP3^{KD}) or APLF (A549-APLF^{KD}), or of both PARP-3 and APLF (A549-PARP3^{KD}/A549-APLF^{KD}), were γ-irradiated (2 Gy). Cells were harvested at the indicated times following irradiation and the average number of γH2AX foci per cell was quantified. Right, Western blot showing APLF, PARP-3, and Actin protein levels in the cells employed above.
[B] A549 cells mock-depleted (A549) or transiently-depleted of APLF (A549-APLF^{KD}) were mock-treated or treated with the PARP inhibitor (PARPi) KU-58948 (500nM) for 30 min as indicated prior to mock-irradiation or γ-irradiation (2 Gy). Cells were harvested at the indicated times following irradiation and the average number of γH2AX foci/cell quantified. Data and statistical analyses are as in Fig.1A.
[C] A549 cells mock-depleted (A549) or transiently-depleted of PARP-1 (A549-PARP1^{KD}) or both APLF and PARP-1 (A549-PARP1^{KD}/APLF^{KD}) were mock-treated or treated with the PARP inhibitor KU-58948 (500nM) for 30 min as indicated (+/-PARPi), prior to mock-irradiation or γ-irradiation (2 Gy). Cells were harvested at the indicated times following irradiation and the average number of γH2AX foci/cell quantified. Data and statistical analyses are as in Fig.1A.

Note that the data in panels B and C, and also panel B of Figure 1, are from the same set of experiments but are presented separately for clarity. The "A549" control and "A549-PARP1^{KD}" data sets in these panels are thus duplicated.

Figure 5: APLF over-expression restores rapid rates of DSBR in PARP-3 depleted cells

[A] A549 cells mock-depleted (A549) or stably-depleted of APLF (A549-APLF^{KD}) were stably-transfected with empty pCI-Puro vector (A549 APLF^{KD} + Vector) or pCI-Puro-construct encoding targeting resistant APLF (A549 APLF^{KD} + APLF^{TR}) or APLF^{Zfm1} harbouring a mutated ADP-ribose binding PBZ domain (A549 APLF^{KD} + APLF Zfm1^{TR}). Cells were mock-irradiated of γ-irradiated (2 Gy), harvested at the indicated times following irradiation and the average number of γH2AX foci/cell quantified. Data and statistical analyses are as in Fig.1A. The bottom panels are Western blots showing APLF levels in the cell lines employed above. An actin blot is included as a loading control.

[B] A549 cells mock-depleted (A549, A549+APLF) or transiently-depleted (A549-PARP3^{KD}, A549- PARP3^{KD} +APLF) of PARP-3 and either mock-complemented (A549, A549-PARP3^{KD}) or complemented (A549+APLF, A549- PARP3^{KD} +APLF) with recombinant human APLF were analysed as described above. The bottom panels are Western blots showing APLF levels in the cell lines employed above. An actin blot is included as a loading control.

Figure 6: APLF promotes XRCC4 retention in damaged chromatin

[A] A549 cells mock-depleted (A549) or stably-depleted of APLF (A549-APLF^{KD}) were transiently-transfected with pEGFP-XRCC4 (green). 24 hr after transfection, transfected cells were locally irradiated with a UVA laser and pEGFP-XRCC4 accumulation at the site of damage quantified for the indicated period (seconds). Data are plotted as the percentage increase in fluorescence (arbitrary units) at the site of UVA irradiation, following irradiation. Data are the mean of >50 cells. Right panel, a representative example of mock-depleted and APLF-depleted cells before and after UVA irradiation.

[B] A549 cells stably-depleted of APLF (A549-APLF^{KD}) and either mock-complemented (A549-APLF^{KD}/Vector) or complemented with targeting-resistant APLF (A549-APLF^{KD}/APLF^{TR}) or targeting-resistant APLF Zfm1 (A549-APLF^{KD}/APLF^{TR}) were transiently-transfected with pEGFP-XRCC4 and analysed as described above.

[C] A549 cells mock-depleted (A549) or stably-depleted of APLF (A549-APLF^{KD}) were mock-irradiated or γ-irradiated (20 Gy) and then fractionated at the times indicated into soluble cellular

(S1) and insoluble/chromatin-bound (P2) protein. Aliquots of each fraction were separated by SDS-PAGE and immunoblotted for the proteins indicated.

Figure 7: The DSBR defect in APLF-depleted and PARP-3-depleted cells is complemented by XRCC4/Lig4 over-expression and impacts on class switch recombination.

[A] A549 cells mock-depleted (WT) or stably-depleted of APLF (APLF KD) were transiently-transfected with expression constructs encoding GFP, GFP-XRCC4, or Lig4 singly or in combination, as indicated. Cells were mock-irradiated or γ-irradiated (2 Gy) 24 hr after transfection and the average number of γH2AX foci/per cell quantified at the indicated times following irradiation. Data and statistical analyses are as in Fig.1, with the exception that the wild-type line against which other data sets are compared is "WT+GFP".

[B] Mock-depleted (WT) or transient-PARP-3-depleted (PARP-3 KD) A549 cells were transiently-transfected with expression constructs encoding GFP or GFP-XRCC4 and Lig4 in combination, as indicated. Cells were mock-irradiated or γ-irradiated (2 Gy) 24 hr after transfection and the average number of γH2AX foci/per cell quantified at the indicated times following irradiation. Data and statistical analyses are as above.

[C] Primary MEFs derived from $Aplf^{+/+}$ ('WT'), $Aplf^{+/-}$ ('HT'), and $Aplf^{-/-}$ ('KO') mouse embryos were mock-irradiated or γ-irradiated (2 Gy) 24 hr after transfection and the average number of γH2AX foci/per cell quantified at the indicated times following irradiation. Data and statistical analyses are as in Fig.1A.

[D] Sμ/Sγ3 switch regions in genomic DNA from cultured $Aplf^{+/+}$ and $Aplf^{-/-}$ splenic mouse B lymphocytes were PCR amplified, cloned, and sequenced. Histograms represent the percentage of Sμ/ Sγ3 class switch junctions with the indicated length of microhomology. The mean length (bp) of microhomology (MH) and the number of sequences analyzed (n) are indicated. Sequences with small insertions (1-3 nucleotides) at the junction were scored as zero microhomology and are shown in white. The difference in mean length of microhomology between $Aplf^{+/+}$ and $Aplf^{-/-}$ class switch junctions was confirmed as statistically significant by Mann-Whitney ($p=0.035$).

[E] Model for PARP-3/APLF Acceleration of NHEJ. PARP-3 is activated at a DSB and autoribosylates itself and trans-ribosylates histone H1 (Top). This event may occur before or

after DNA-PK dependent events. APLF is then recruited to DSBs via binding of its PBZ domain to ribosylated histone H1 (middle), and thereby renders chromatin more 'permissive' for DNA ligation (bottom). APLF renders chromatin 'permissive' by promoting XRCC4/Lig4 retention in chromatin, either by direct interaction with XRCC4 and/or by modifying chromatin structure directly. Yellow ovals with blue lines denote nucleosomes and DNA, respectively, and blue ovals denote histone H1. Red lines denote mADPr/pADPr.

References

Ahel, I., Ahel, D., Matsusaka, T., Clark, A.J., Pines, J., Boulton, S.J., and West, S.C. (2008). Poly(ADP-ribose)-binding zinc finger motifs in DNA repair/checkpoint proteins. Nature 451, 81-85.

Ame, J.C., Spenlehauer, C., and de Murcia, G. (2004). The PARP superfamily. Bioessays 26, 882-893.

Audebert, M., Salles, B., and Calsou, P. (2004). Involvement of poly(ADP-ribose) polymerase-1 and XRCC1/DNA ligase III in an alternative route for DNA double-strand breaks rejoining. J Biol Chem 279, 55117-55126.

Bekker-Jensen, S., Fugger, K., Danielsen, J.R., Gromova, I., Sehested, M., Celis, J., Bartek, J., Lukas, J., and Mailand, N. (2007). Human Xip1 (C2orf13) is a novel regulator of cellular responses to DNA strand breaks. J Biol Chem 282, 19638-19643.

Benjamin, R.C., and Gill, D.M. (1980). Poly(ADP-ribose) synthesis in vitro programmed by damaged DNA. A comparison of DNA molecules containing different types of strand breaks. J Biol Chem 255, 10502-10508.

Boulton, S., Kyle, S., and Durkacz, B.W. (1999). Interactive effects of inhibitors of poly(ADP-ribose) polymerase and DNA-dependent protein kinase on cellular responses to DNA damage. Carcinogenesis 20, 199-203.

Brown, M.L., Franco, D., Burkle, A., and Chang, Y. (2002). Role of poly(ADP-ribosyl)ation in DNA-PKcs- independent V(D)J recombination. Proc Natl Acad Sci U S A 99, 4532-4537.

Bryant, H.E., Petermann, E., Schultz, N., Jemth, A.S., Loseva, O., Issaeva, N., Johansson, F., Fernandez, S., McGlynn, P., and Helleday, T. (2009). PARP is activated at stalled forks to mediate Mre11-dependent replication restart and recombination. EMBO J 28, 2601-2615.

Bryant, H.E., Schultz, N., Thomas, H.D., Parker, K.M., Flower, D., Lopez, E., Kyle, S., Meuth, M., Curtin, N.J., and Helleday, T. (2005). Specific killing of BRCA2-deficient tumours with inhibitors of poly(ADP-ribose) polymerase. Nature 434, 913-917.

Caldecott, K.W., McKeown, C.K., Tucker, J.D., Ljungquist, S., and Thompson, L.H. (1994). An interaction between the mammalian DNA repair protein XRCC1 and DNA ligase III. Mol Cell Biol 14, 68-76.

Caldecott, K.W., Tucker, J.D., Stanker, L.H., and Thompson, L.H. (1995). Characterization of the XRCC1-DNA ligase III complex in vitro and its absence from mutant hamster cells. Nucleic Acids Res 23, 4836-4843.

Critchlow, S.E., Bowater, R.P., and Jackson, S.P. (1997). Mammalian DNA double-strand break repair protein XRCC4 interacts with DNA ligase IV. Curr Biol 7, 588-598.

Ding, R., Pommier, Y., Kang, V.H., and Smulson, M. (1992). Depletion of poly(ADP-ribose) polymerase by antisense RNA expression results in a delay in DNA strand break rejoining. J Biol Chem 267, 12804-12812.

Drouet, J., Delteil, C., Lefrancois, J., Concannon, P., Salles, B., and Calsou, P. (2005). DNA-dependent protein kinase and XRCC4-DNA ligase IV mobilization in the cell in response to DNA double strand breaks. J Biol Chem 280, 7060-7069.

El-Khamisy, S.F., Masutani, M., Suzuki, H., and Caldecott, K.W. (2003). A requirement for PARP-1 for the assembly or stability of XRCC1 nuclear foci at sites of oxidative DNA damage. Nucleic Acids Res 31, 5526-5533.

Farmer, H., McCabe, N., Lord, C.J., Tutt, A.N., Johnson, D.A., Richardson, T.B., Santarosa, M., Dillon, K.J., Hickson, I., Knights, C., et al. (2005). Targeting the DNA repair defect in BRCA mutant cells as a therapeutic strategy. Nature 434, 917-921.

Fisher, A.E., Hochegger, H., Takeda, S., and Caldecott, K.W. (2007). Poly(ADP-ribose) polymerase 1 accelerates single-strand break repair in concert with poly(ADP-ribose) glycohydrolase. Mol Cell Biol 27, 5597-5605.

Grawunder, U., Wilm, M., Wu, X., Kulesza, P., Wilson, T.E., Mann, M., and Lieber, M.R. (1997). Activity of DNA ligase IV stimulated by complex formation with XRCC4 protein in mammalian cells. Nature 388, 492-495.

Hochegger, H., Dejsuphong, D., Fukushima, T., Morrison, C., Sonoda, E., Schreiber, V., Zhao, G.Y., Saberi, A., Masutani, M., Adachi, N., et al. (2006). Parp-1 protects homologous recombination from interference by Ku and Ligase IV in vertebrate cells. EMBO J 25, 1305-1314.

Hottiger, M.O., Hassa, P.O., Luscher, B., Schuler, H., and Koch-Nolte, F. (2010). Toward a unified nomenclature for mammalian ADP-ribosyltransferases. Trends Biochem Sci.

Iles, N., Rulten, S., El-Khamisy, S.F., and Caldecott, K.W. (2007). APLF (C2orf13) is a novel human protein involved in the cellular response to chromosomal DNA strand breaks. Mol Cell Biol 27, 3793-3803.

Kanno, S., Kuzuoka, H., Sasao, S., Hong, Z., Lan, L., Nakajima, S., and Yasui, A. (2007). A novel human AP endonuclease with conserved zinc-finger-like motifs involved in DNA strand break responses. Embo J 26, 2094-2103.

Kickhoefer, V.A., Siva, A.C., Kedersha, N.L., Inman, E.M., Ruland, C., Streuli, M., and Rome, L.H. (1999). The 193-kD vault protein, VPARP, is a novel poly(ADP-ribose) polymerase. J Cell Biol 146, 917-928.

Kleine, H., Poreba, E., Lesniewicz, K., Hassa, P.O., Hottiger, M.O., Litchfield, D.W., Shilton, B.H., and Luscher, B. (2008). Substrate-assisted catalysis by PARP10 limits its activity to mono-ADP-ribosylation. Mol Cell 32, 57-69.

Le Page, F., Schreiber, V., Dherin, C., De Murcia, G., and Boiteux, S. (2003). Poly(ADP-ribose) polymerase-1 (PARP-1) is required in murine cell lines for base excision repair of oxidative DNA damage in the absence of DNA polymerase beta. J Biol Chem 278, 18471-18477.

Lehtio, L., Jemth, A.S., Collins, R., Loseva, O., Johansson, A., Markova, N., Hammarstrom, M., Flores, A., Holmberg-Schiavone, L., Weigelt, J., et al. (2009). Structural basis for inhibitor specificity in human poly(ADP-ribose) polymerase-3. J Med Chem 52, 3108-3111.

Lobrich, M., Shibata, A., Beucher, A., Fisher, A., Ensminger, M., Goodarzi, A.A., Barton, O., and Jeggo, P.A. (2010). gammaH2AX foci analysis for monitoring DNA double-strand break repair: strengths, limitations and optimization. Cell Cycle 9, 662-669.

Loseva, O., Jemth, A.S., Bryant, H.E., Schuler, H., Lehtio, L., Karlberg, T., and Helleday, T. (2010). Poly(ADP-ribose) polymerase-3 (PARP-3) is a mono-ADP ribosylase that activates PARP-1 in absence of DNA. J Biol Chem.

Macrae, C.J., McCulloch, R.D., Ylanko, J., Durocher, D., and Koch, C.A. (2008). APLF (C2orf13) facilitates nonhomologous end-joining and undergoes ATM-dependent hyperphosphorylation following ionizing radiation. DNA Repair (Amst) 7, 292-302.

Mahaney, B.L., Meek, K., and Lees-Miller, S.P. (2009). Repair of ionizing radiation-induced DNA double-strand breaks by non-homologous end-joining. Biochem J 417, 639-650.

Morrison, C., Smith, G.C., Stingl, L., Jackson, S.P., Wagner, E.F., and Wang, Z.Q. (1997). Genetic interaction between PARP and DNA-PK in V(D)J recombination and tumorigenesis. Nat Genet 17, 479-482.

Okano, S., Lan, L., Caldecott, K.W., Mori, T., and Yasui, A. (2003). Spatial and temporal cellular responses to single-strand breaks in human cells. Mol Cell Biol 23, 3974-3981.

Otto, H., Reche, P.A., Bazan, F., Dittmar, K., Haag, F., and Koch-Nolte, F. (2005). In silico characterization of the family of PARP-like poly(ADP-ribosyl)transferases (pARTs). BMC Genomics 6, 139.

Poirier, G.G., de Murcia, G., Jongstra-Bilen, J., Niedergang, C., and Mandel, P. (1982). Poly(ADP-ribosyl)ation of polynucleosomes causes relaxation of chromatin structure. Proc Natl Acad Sci U S A 79, 3423-3427.

Robert, I., Dantzer, F., and Reina-San-Martin, B. (2009). Parp1 facilitates alternative NHEJ, whereas Parp2 suppresses IgH/c-myc translocations during immunoglobulin class switch recombination. J Exp Med 206, 1047-1056.

Roberts, S.A., Strande, N., Burkhalter, M.D., Strom, C., Havener, J.M., Hasty, P., and Ramsden, D.A. (2010). Ku is a 5'-dRP/AP lyase that excises nucleotide damage near broken ends. Nature 464, 1214-1217.

Rogakou, E.P., Boon, C., Redon, C., and Bonner, W.M. (1999). Megabase chromatin domains involved in DNA double-strand breaks in vivo. J Cell Biol 146, 905-916.

Rogakou, E.P., Pilch, D.R., Orr, A.H., Ivanova, V.S., and Bonner, W.M. (1998). DNA double-stranded breaks induce histone H2AX phosphorylation on serine 139. J Biol Chem 273, 5858-5868.

Rouleau, M., McDonald, D., Gagne, P., Ouellet, M.E., Droit, A., Hunter, J.M., Dutertre, S., Prigent, C., Hendzel, M.J., and Poirier, G.G. (2007). PARP-3 associates with polycomb group bodies and with components of the DNA damage repair machinery. J Cell Biochem 100, 385-401.

Rulten, S.L., Cortes-Ledesma, F., Guo, L., Iles, N.J., and Caldecott, K.W. (2008). APLF (C2orf13) is a novel component of poly(ADP-ribose) signaling in mammalian cells. Mol Cell Biol 28, 4620-4628.

Smith, S., Giriat, I., Schmitt, A., and de Lange, T. (1998). Tankyrase, a poly(ADP-ribose) polymerase at human telomeres. Science 282, 1484-1487.

Soulas-Sprauel, P., Le Guyader, G., Rivera-Munoz, P., Abramowski, V., Olivier-Martin, C., Goujet-Zalc, C., Charneau, P., and de Villartay, J.P. (2007). Role for DNA repair factor XRCC4 in immunoglobulin class switch recombination. J Exp Med 204, 1717-1727.

Stevnsner, T., Ding, R., Smulson, M., and Bohr, V.A. (1994). Inhibition of gene-specific repair of alkylation damage in cells depleted of poly(ADP-ribose) polymerase. Nucleic Acids Res 22, 4620-4624.

Sugimura, K., Takebayashi, S., Taguchi, H., Takeda, S., and Okumura, K. (2008). PARP-1 ensures regulation of replication fork progression by homologous recombination on damaged DNA. J Cell Biol 183, 1203-1212.

Trucco, C., Oliver, F.J., de Murcia, G., and Menissier-de Murcia, J. (1998). DNA repair defect in poly(ADP-ribose) polymerase-deficient cell lines. Nucleic Acids Res 26, 2644-2649.

Wang, M., Wu, W., Rosidi, B., Zhang, L., Wang, H., and Iliakis, G. (2006). PARP-1 and Ku compete for repair of DNA double strand breaks by distinct NHEJ pathways. Nucleic Acids Res 34, 6170-6182.

Yan, C.T., Boboila, C., Souza, E.K., Franco, S., Hickernell, T.R., Murphy, M., Gumaste, S., Geyer, M., Zarrin, A.A., Manis, J.P., et al. (2007). IgH class switching and translocations use a robust non-classical end-joining pathway. Nature 449, 478-482.

Yang, Y.G., Cortes, U., Patnaik, S., Jasin, M., and Wang, Z.Q. (2004). Ablation of PARP-1 does not interfere with the repair of DNA double-strand breaks, but compromises the reactivation of stalled replication forks. Oncogene 23, 3872-3882.

Yano, K., and Chen, D.J. (2008). Live cell imaging of XLF and XRCC4 reveals a novel view of protein assembly in the non-homologous end-joining pathway. Cell Cycle 7, 1321-1325.

Yano, K., Morotomi-Yano, K., Wang, S.Y., Uematsu, N., Lee, K.J., Asaithamby, A., Weterings, E., and Chen, D.J. (2008). Ku recruits XLF to DNA double-strand breaks. EMBO Rep 9, 91-96.

Figure 1

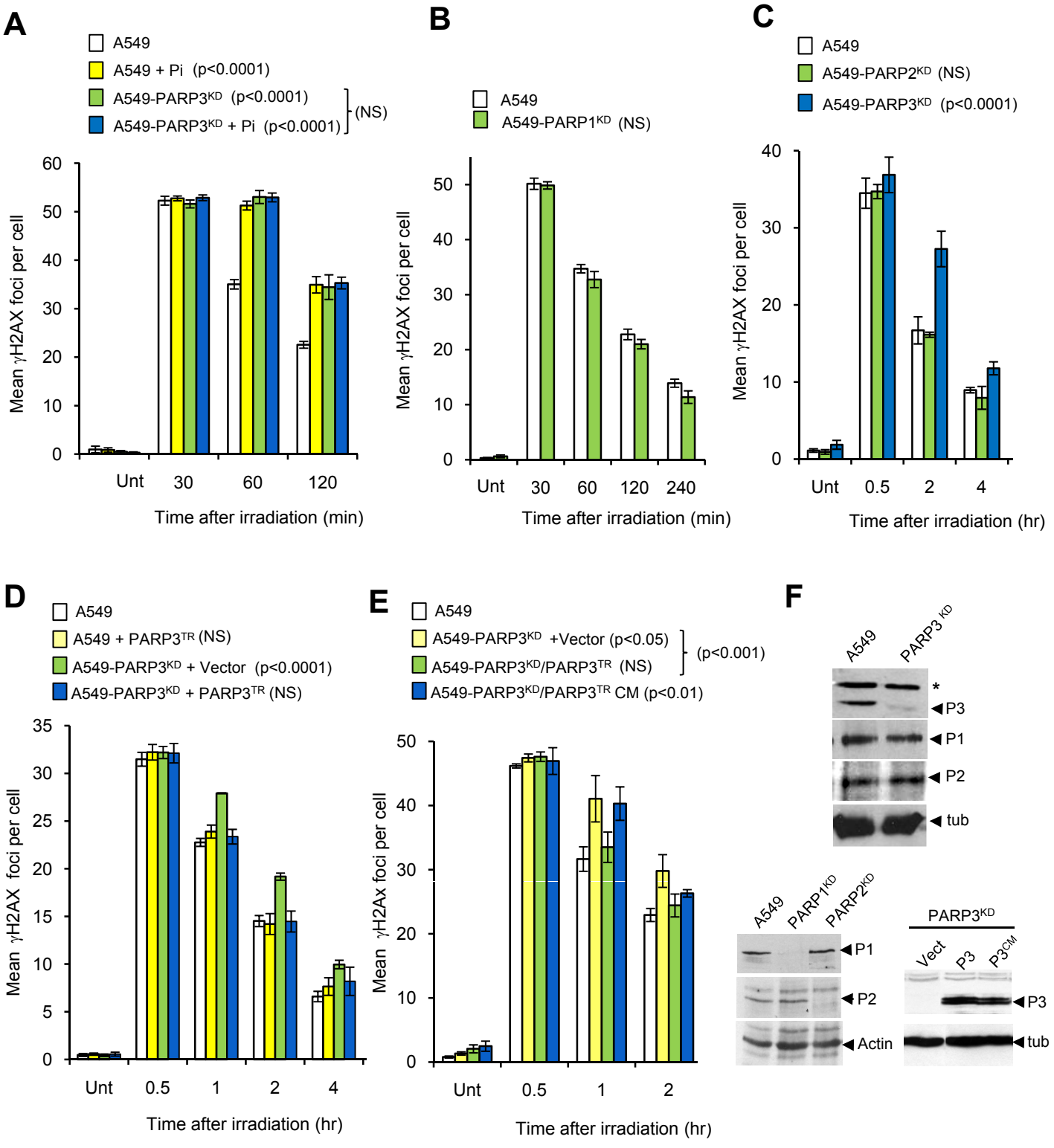
A
A549
A549 + Pi (p<0.0001)
A549-PARP3KD (p<0.0001)
A549-PARP3KD + Pi (p<0.0001)
(NS)
Mean γH2AX foci per cell
Unt
30
60
120
Time after irradiation (min)
B
A549
A549-PARP1KD (NS)
Mean γH2AX foci per cell
Unt
30
60
120
240
Time after irradiation (min)
C
A549
A549-PARP2KD (NS)
A549-PARP3KD (p<0.0001)
Mean γH2AX foci per cell
Unt
0.5
2
4
Time after irradiation (hr)
D
A549
A549 + PARP3TR (NS)
A549-PARP3KD + Vector (p<0.0001)
A549-PARP3KD + PARP3TR (NS)
Mean γH2AX foci per cell
Unt
0.5
1
2
4
Time after irradiation (hr)
E
A549
A549-PARP3KD +Vector (p<0.05)
A549-PARP3KD/PARP3TR (NS)
(p<0.001)
A549-PARP3KD/PARP3TR CM (p<0.01)
Mean γH2Ax foci per cell
Unt
0.5
1
2
Time after irradiation (hr)
F
A549
PARP3 KD
*
P3
P1
P2
tub
A549
PARP1KD
PARP2KD
P1
P2
Actin
PARP3KD
Vect
P3
P3CM
P3
tub

Figure 2

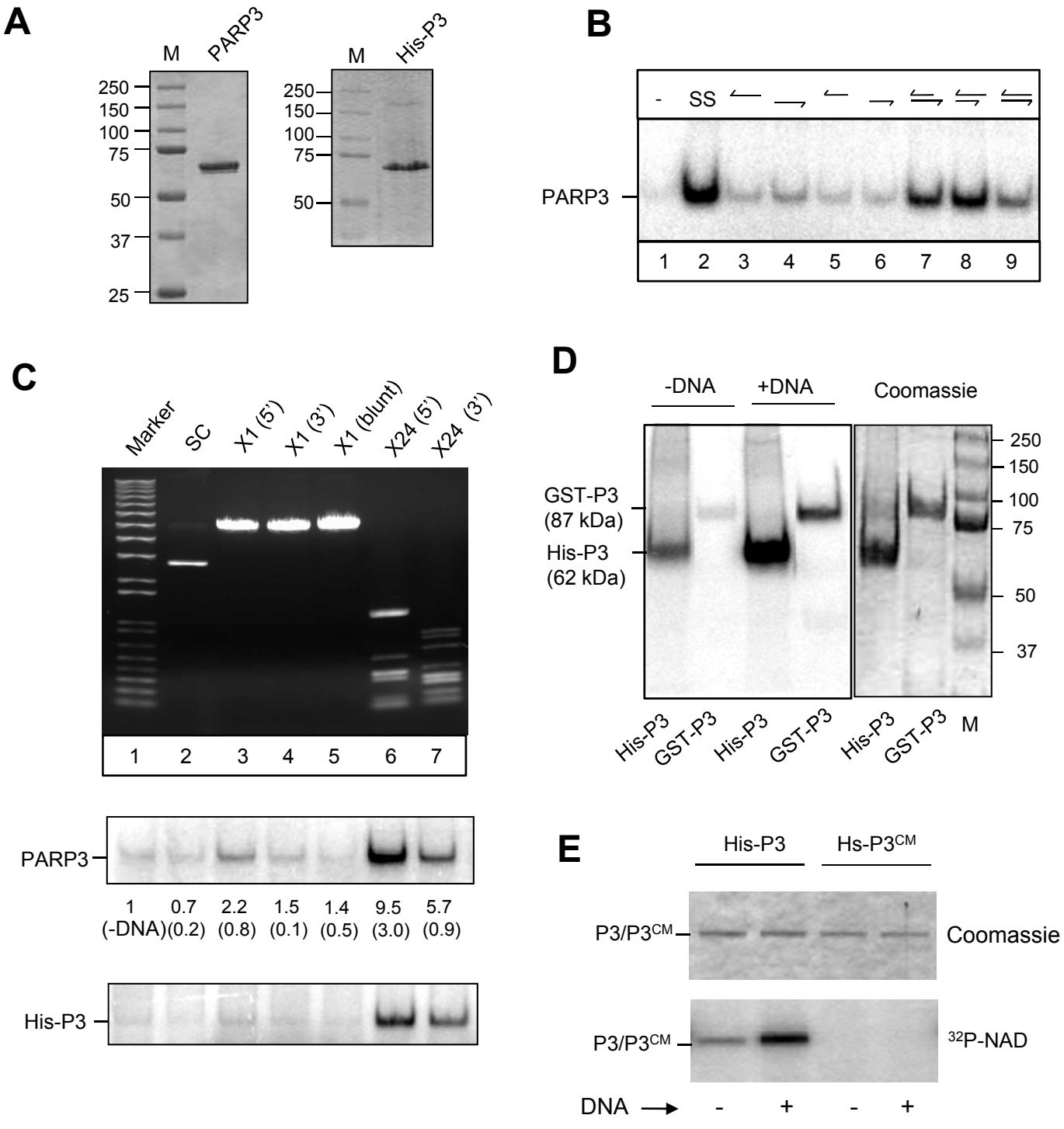
A
M
PARP3
250
150
100
75
50
37
25
M
His-P3
250
150
100
75
50
B
-
SS
PARP3
1 2 3 4 5 6 7 8 9
C
Marker
SC
X1 (5')
X1 (3')
X1 (blunt)
X24 (5')
X24 (3')
1 2 3 4 5 6 7
PARP3
1 (-DNA)
0.7 (0.2)
2.2 (0.8)
1.5 (0.1)
1.4 (0.5)
9.5 (3.0)
5.7 (0.9)
His-P3
D
-DNA
+DNA
Coomassie
GST-P3 (87 kDa)
His-P3 (62 kDa)
250
150
100
75
50
37
His-P3
GST-P3
His-P3
GST-P3
His-P3
GST-P3
M
E
His-P3
Hs-P3CM
P3/P3CM
Coomassie
P3/P3CM
32P-NAD
DNA → - + - +

Figure 3

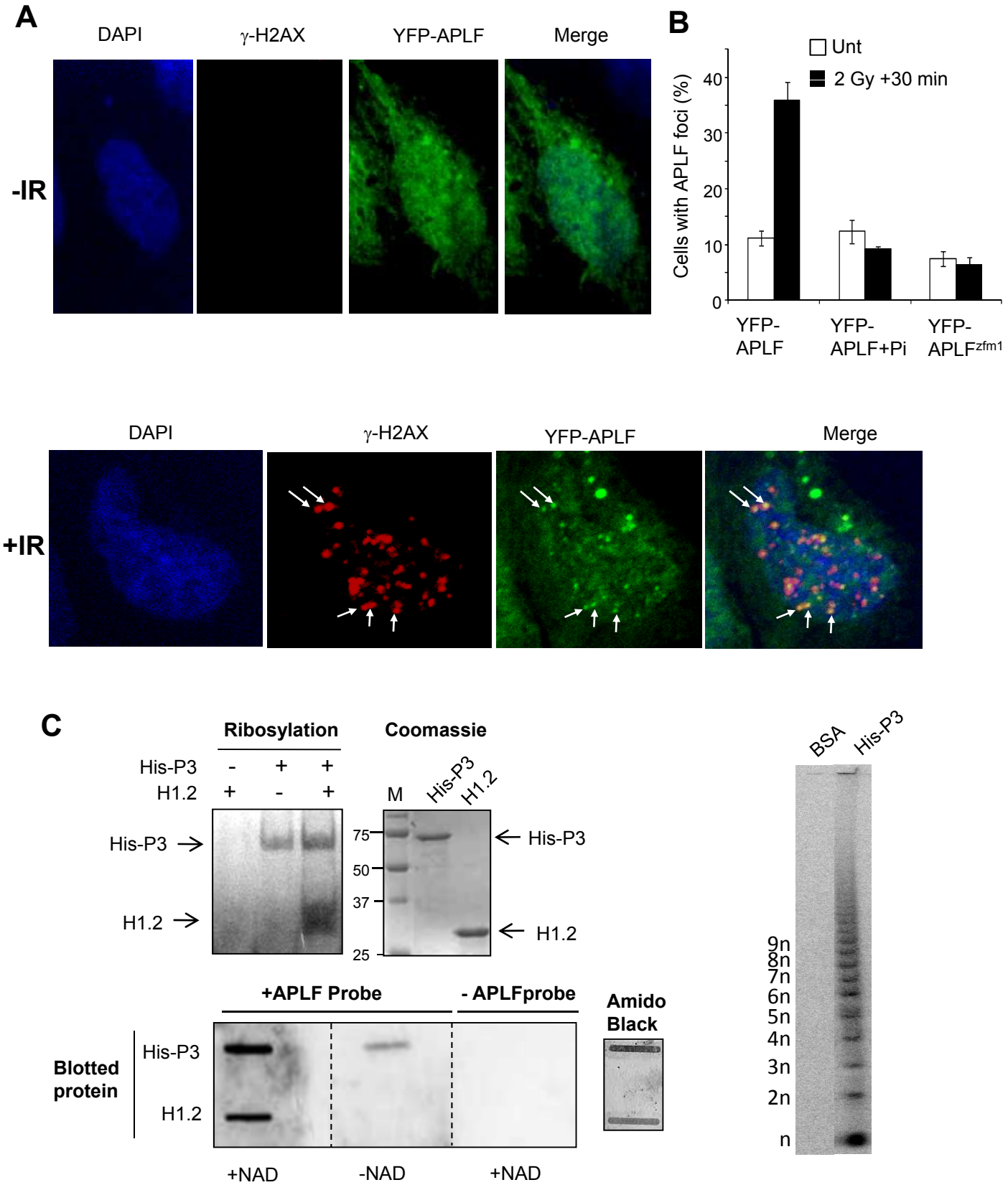
A
DAPI
γ-H2AX
YFP-APLF
Merge
-IR
+IR
B
Unt
2 Gy +30 min
Cells with APLF foci (%)
0
10
20
30
40
YFP-APLF
YFP-APLF+Pi
YFP-APLFzfm1
C
Ribosylation
Coomassie
His-P3
H1.2
M
75
50
37
25
+APLF Probe
- APLFprobe
Amido Black
Blotted protein
+NAD
-NAD
+NAD
BSA
9n
8n
7n
6n
5n
4n
3n
2n
n

Figure 4

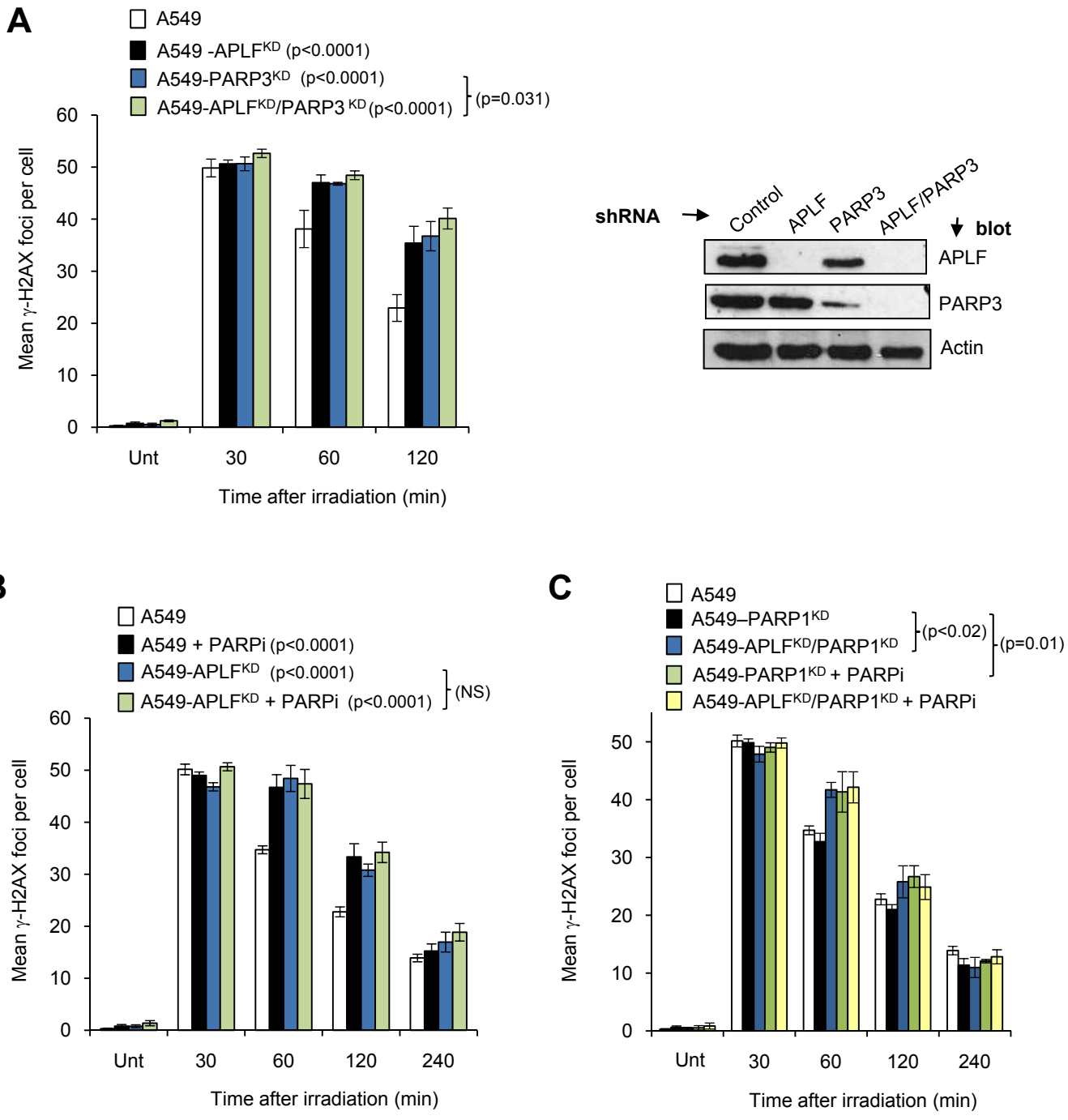
A
A549
A549 -APLF^KD (p<0.0001)
A549-PARP3^KD (p<0.0001)
A549-APLF^KD/PARP3^KD (p<0.0001)
(p=0.031)
Mean γ-H2AX foci per cell
0
10
20
30
40
50
60
Unt
30
60
120
Time after irradiation (min)
shRNA
Control
APLF
PARP3
APLF/PARP3
blot
APLF
PARP3
Actin
B
A549
A549 + PARPi (p<0.0001)
A549-APLF^KD (p<0.0001)
A549-APLF^KD + PARPi (p<0.0001)
(NS)
Mean γ-H2AX foci per cell
0
10
20
30
40
50
60
Unt
30
60
120
240
Time after irradiation (min)
C
A549
A549–PARP1^KD
A549-APLF^KD/PARP1^KD
(p<0.02)
(p=0.01)
A549-PARP1^KD + PARPi
A549-APLF^KD/PARP1^KD + PARPi
Mean γ-H2AX foci per cell
0
10
20
30
40
50
Unt
30
60
120
240
Time after irradiation (min)

Figure 5

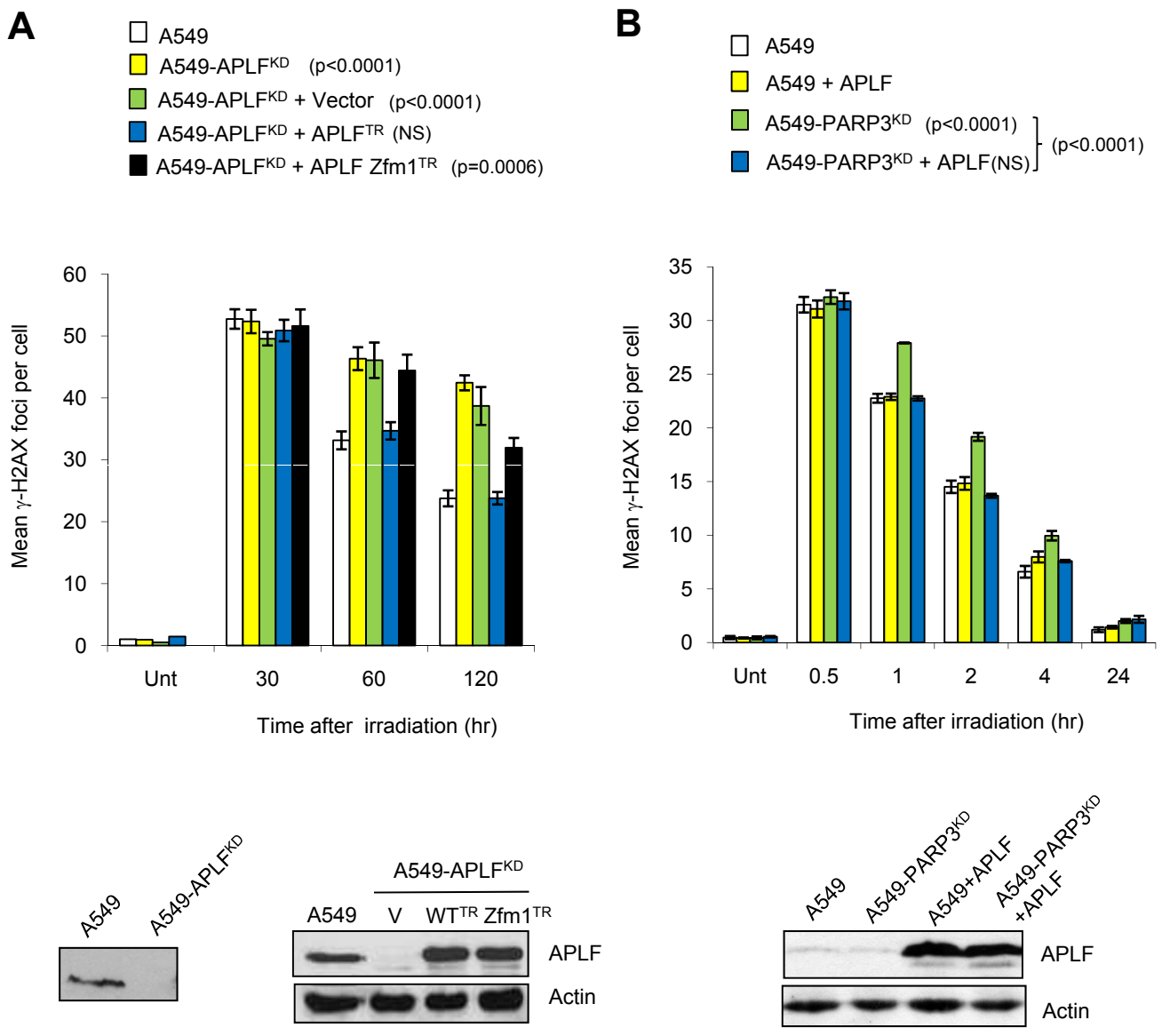
A
A549
A549-APLF^KD (p<0.0001)
A549-APLF^KD + Vector (p<0.0001)
A549-APLF^KD + APLF^TR (NS)
A549-APLF^KD + APLF Zfm1^TR (p=0.0006)
Mean γ-H2AX foci per cell
0
10
20
30
40
50
60
Unt
30
60
120
Time after irradiation (hr)
B
A549
A549 + APLF
A549-PARP3^KD (p<0.0001)
A549-PARP3^KD + APLF(NS)
(p<0.0001)
Mean γ-H2AX foci per cell
0
5
10
15
20
25
30
35
Unt
0.5
1
2
4
24
Time after irradiation (hr)
A549
A549-APLF^KD
A549-APLF^KD
A549
V
WT^TR Zfm1^TR
APLF
Actin
A549
A549-PARP3^KD
A549+APLF
A549-PARP3^KD +APLF
APLF
Actin

Figure 6

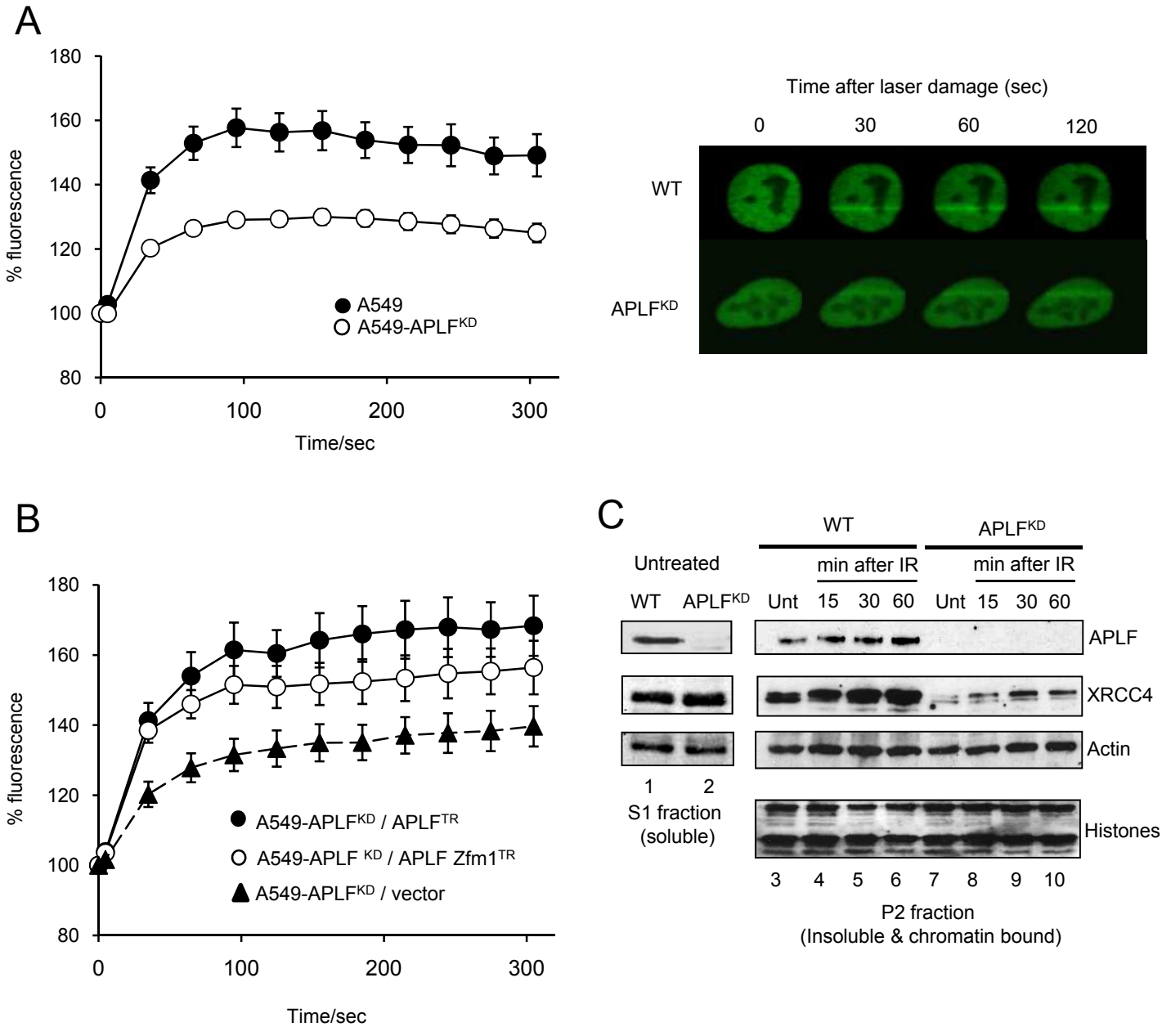
A
% fluorescence
Time/sec
A549
A549-APLF^KD
Time after laser damage (sec)
0
30
60
120
WT
APLF^KD
B
% fluorescence
Time/sec
A549-APLF^KD / APLF^TR
A549-APLF ^KD / APLF Zfm1^TR
A549-APLF^KD / vector
C
Untreated
WT
APLF^KD
min after IR
Unt
15
30
60
APLF
XRCC4
Actin
Histones
S1 fraction
(soluble)
P2 fraction
(Insoluble & chromatin bound)

Figure 7

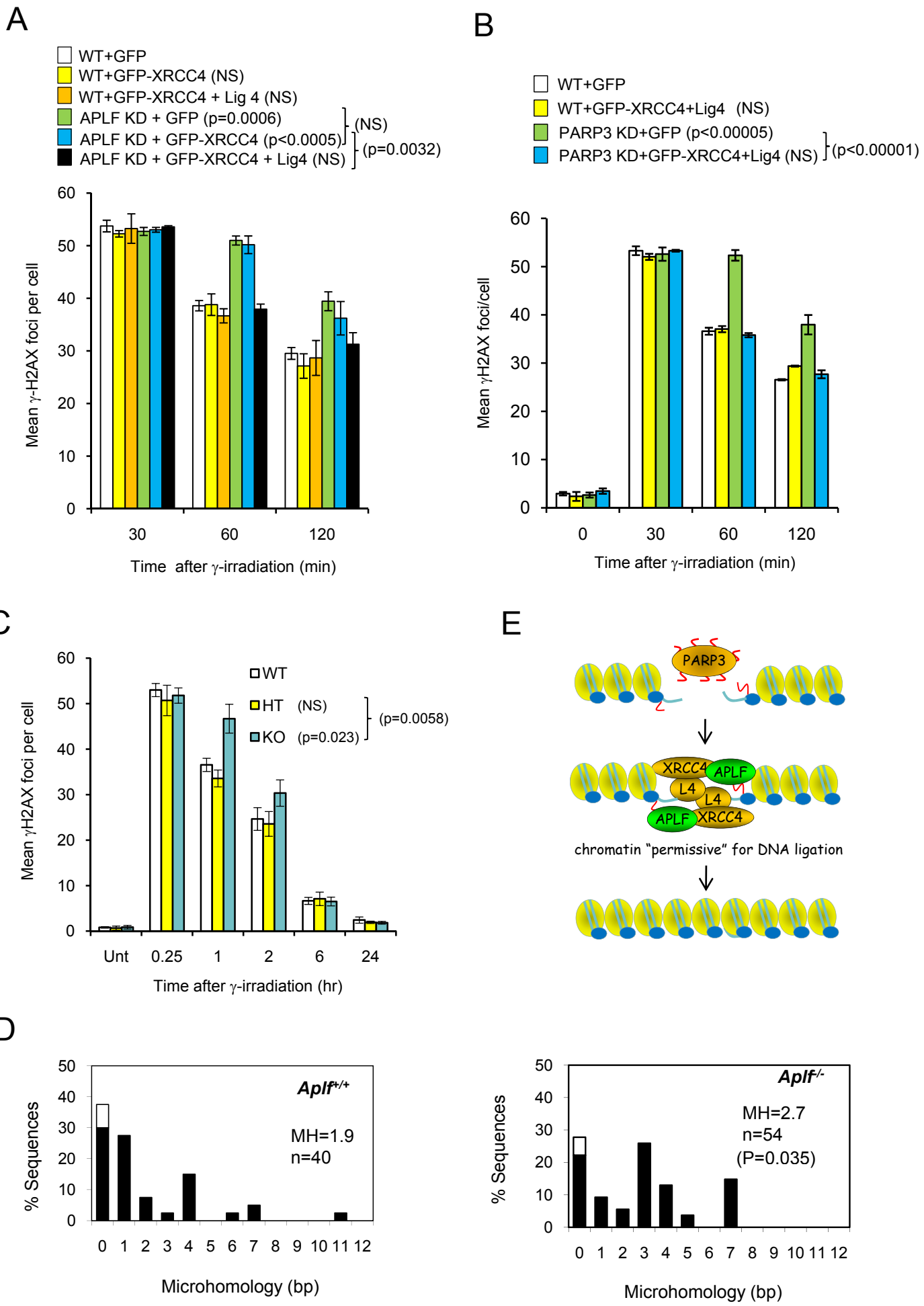
A
WT+GFP
WT+GFP-XRCC4 (NS)
WT+GFP-XRCC4 + Lig 4 (NS)
APLF KD + GFP (p=0.0006)
APLF KD + GFP-XRCC4 (p<0.0005)
APLF KD + GFP-XRCC4 + Lig4 (NS)
(NS)
(p=0.0032)
Mean γ-H2AX foci per cell
Time after γ-irradiation (min)
B
WT+GFP
WT+GFP-XRCC4+Lig4 (NS)
PARP3 KD+GFP (p<0.00005)
PARP3 KD+GFP-XRCC4+Lig4 (NS)
(p<0.00001)
Mean γH2AX foci/cell
Time after γ-irradiation (min)
C
WT
HT (NS)
KO (p=0.023)
(p=0.0058)
Mean γH2AX foci per cell
Unt
Time after γ-irradiation (hr)
E
PARP3
XRCC4
APLF
L4
chromatin "permissive" for DNA ligation
D
Aplf+/+
MH=1.9
n=40
% Sequences
Microhomology (bp)
Aplf-/-
MH=2.7
n=54
(P=0.035)

Inventory of supplementary information

Supplementary Figure 1; This figure contains a represenatative image of the γ-ray induced γ-H2AX foci counted in this work to quantify DSBR (panel A). The figure also provides evidence that KU58948 inhibits PARP-3 activity at the concentration employed in our experiments (500nM)(panel B). The figure also includes evidence that APLF depletion reduces DSBR in A549 cells irradiated in G1 and G2 (panel C), and that PARP-3 depletion does not reduce global levels of PARP activity (panel D).

Supplementary Figure 2; This figure demonstrates that the preparation of PARP-3 (Alexis) employed in Fig.2B & C does not contain contaminating PARP-1.

Supplementary Figure 3; This figure describes the Aplf-/- mouse model employed here to create MEFs and B cells for analysis.

Supplementary Figure 4; This figure demonstrates that global frequencies of class-switch recombination are normal in $Aplf^{-/-}$ B cells.

Supplementary Figure 5; This figure includes representative sequences at class-switch recombination in WT and $Aplf^{-/-}$ B cells.

Supplementary Figure 6; This figure includes evidence that PARP-3 also promotes repair of etoposide-induced DSBs.

Inventory of supplementary information

Supplementary Figure 1; This figure contains a represenatative image of the γ-ray induced γ-H2AX foci counted in this work to quantify DSBR (panel A). The figure also provides evidence that KU58948 inhibits PARP-3 activity at the concentration employed in our experiments (500nM)(panel B). The figure also includes evidence that APLF depletion reduces DSBR in A549 cells irradiated in G1 and G2 (panel C), and that PARP-3 depletion does not reduce global levels of PARP activity (panel D).

Supplementary Figure 2; This figure demonstrates that the preparation of PARP-3 (Alexis) employed in Fig.2B & C does not contain contaminating PARP-1.

Supplementary Figure 3; This figure describes the Aplf-/- mouse model employed here to create MEFs and B cells for analysis.

Supplementary Figure 4; This figure demonstrates that global frequencies of class-switch recombination are normal in $Aplf^{-/-}$ B cells.

Supplementary Figure 5; This figure includes representative sequences at class-switch recombination in WT and $Aplf^{-/-}$ B cells.

Supplementary Figure 6; This figure includes evidence that PARP-3 also promotes repair of etoposide-induced DSBs.

Supplementary Material

Supplementary Fig1

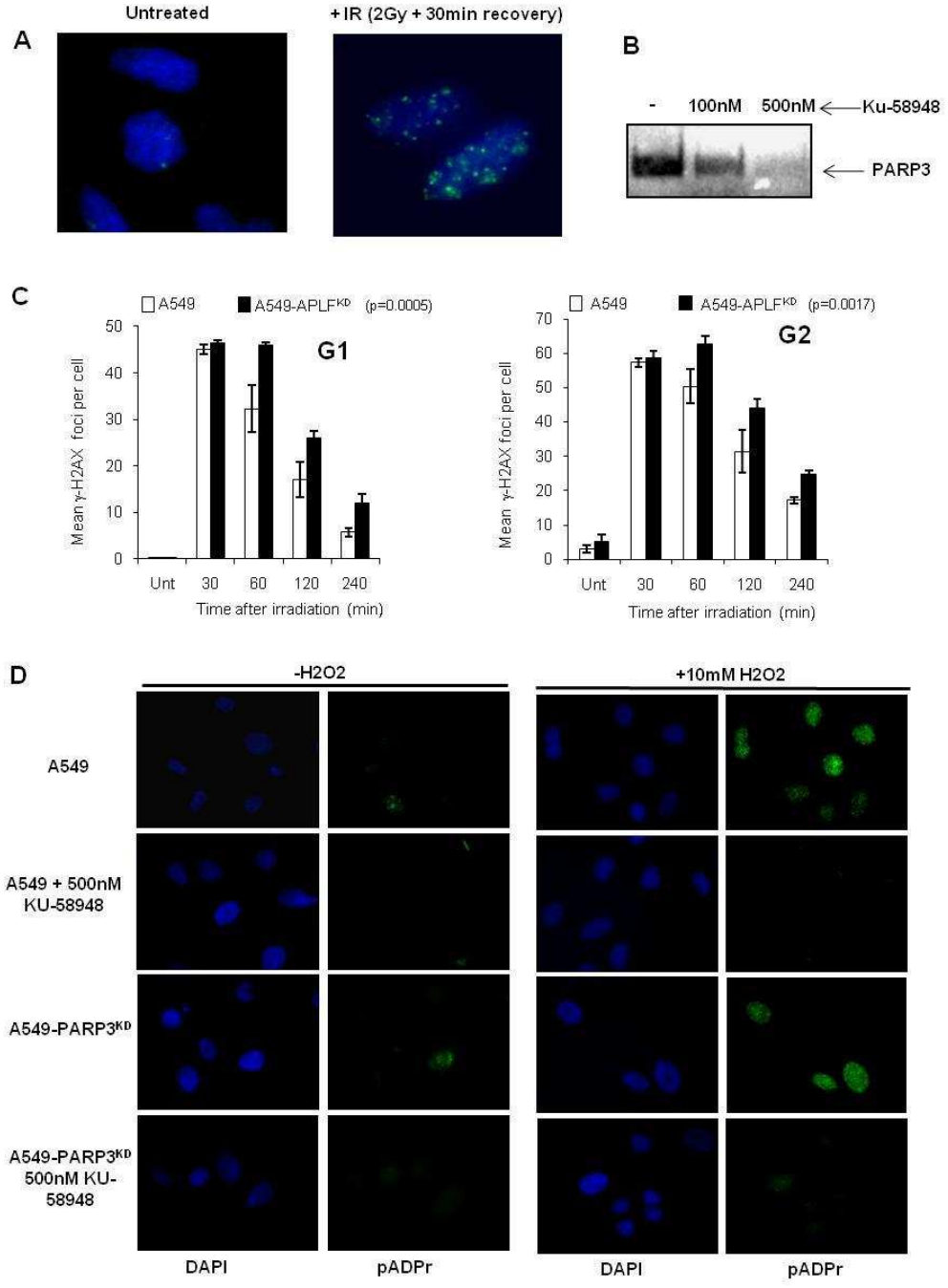

Figure S1: γ-ray induced γH2AX foci and PARP-3 Activity.

[A] Representative images of untreated A549 cells (left) or A549 cells 30 min after 2Gy γ-radiation (right), immunostained for γH2AX (green) and counterstained with DAPI (blue).

[B] Inhibition of PARP-3 by KU-58948 in vitro. 125nM PARP-3 was incubated with 80μM NAD^+, 250nM ^{32}P-NAD^+, and 100ng pEGFP-C2 plasmid cut at 24 sites per molecule with Sau3AI. Reaction products were analysed by SDS acid-PAGE and autoradiaography.

[C] Mock-depleted (A549) or stably APLF-depleted (A549-$APLF^{KD}$) A549 cells were left untreated or were γ-irradiated (2Gy, left panel; 1Gy, right panel). The average number of γH2AX foci per cell was quantified in untreated cells (Unt) and in γ-irradiated cells harvested at the indicated times following irradiation in CENPF-negative cells (G1) and CENPF-positive cells (G2).

[D] Representative images of mock-depleted or PARP-3-depleted A549 cells 1 min after treatment with 10mM H_2O_2 to induce PARP-1 and PARP-2 dependent pADPr synthesis. Cells were pre-incubated or not, as indicated, with 500nM KU-58948 for 30 min prior to treatment. pADPr was detected with anti-pADPr antibody 10H (green) and DNA was counterstained with DAPI (blue).

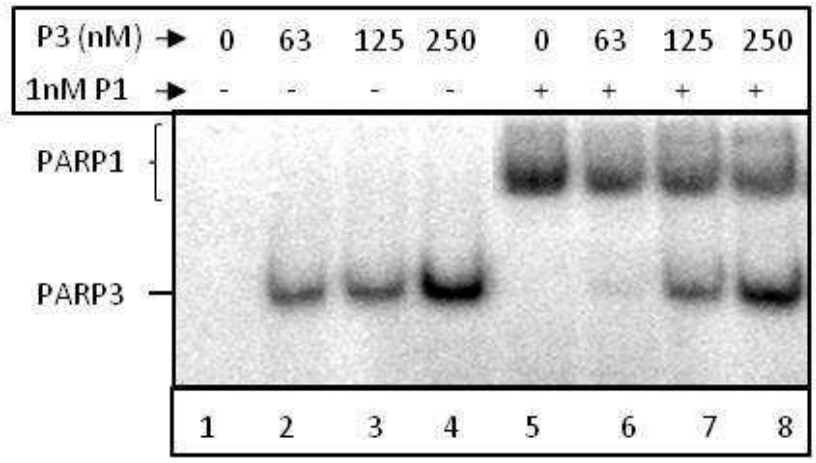

Figure S2: PARP-3 is stimulated by DSBs

[A] The indicated amount of recombinant human PARP-3 (Alexis) was incubated with 0.5μM ^{32}P-NAD$^+$/2μM NAD$^+$ in the presence of 50 ng sonicated salmon sperm DNA and in the presence or absence of 1nM PARP-1 as indicated. Reaction products were analysed as described in Fig.2.

Supplementary Figure 3

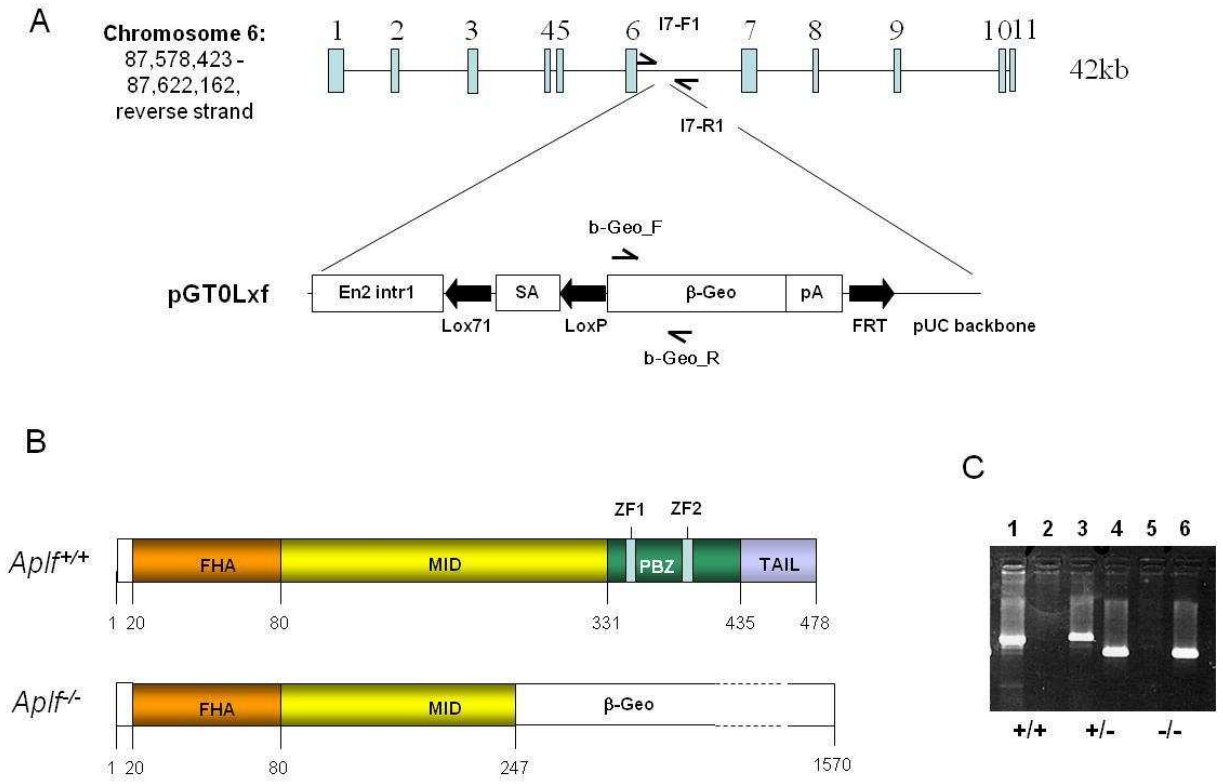

Figure S3: Generation of Aplf$^{-/-}$ mice

[A] Schematic representation of the gene-trap pGT0Lxf insertion into intron 7 of the mouse Aplf chromosomal sequence. Primers used for genotyping are shown: I7_F and I7_R span the insertion site and were used to detect the wild-type Aplf allele, whereas bGeo_F and bGeo_R were used to detect insertion of the bGeo cassette in the disrupted allele. En2Intr1 = 1.5 kb of Mouse En2 intron 1; SA = splice acceptor site; Lox71, LoxP and FRT sites enable reversion of the gene-trap using Cre or Flp recombinase.

[B] Predicted Aplf protein structure resulting from wild-type (WT) and knockout (KO) alleles.

[C] Representative genotyping result for Aplf$^{+/+}$, Aplf$^{+/-}$, and Aplf$^{-/-}$ using I7_F and I7_R (lanes 1, 3 and 5) or bGeo_F and bGeo_R (lanes 2, 4 and 6) primers.

A

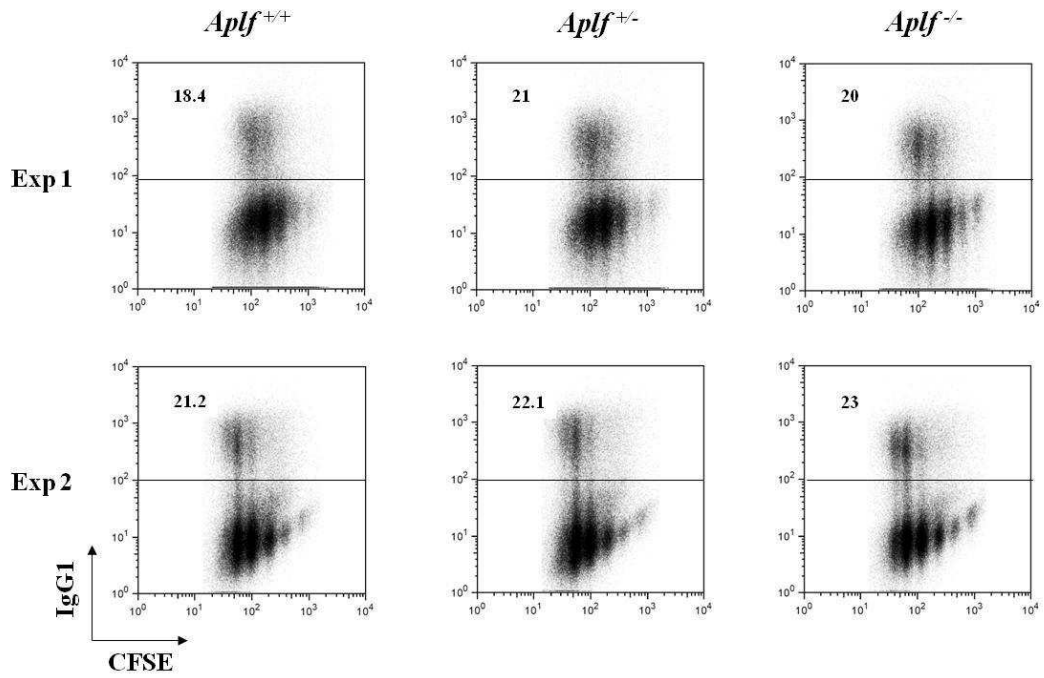

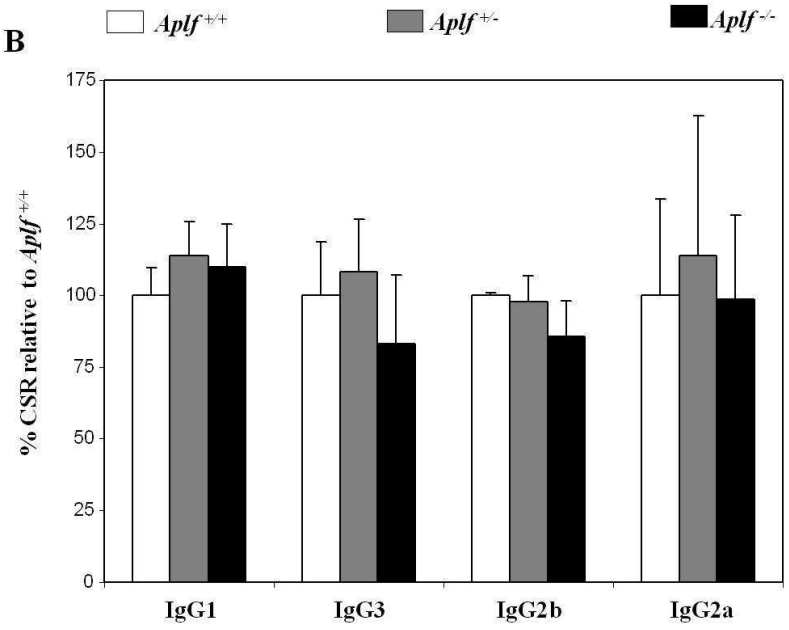

Figure S4: Normal frequencies of class switch recombination in Aplf$^{-/-}$ mouse splenic B cells.

[A] FACS analysis for IgG1 cell surface expression in Aplf$^{+/+}$, Aplf$^{+/-}$, and Aplf$^{-/-}$ splenic B lymphocytes stimulated with LPS + IL-4. The percentage of IgG1+ cells is indicated in each plot.

Cell division was measured by CFSE dye dilution. Top and bottom panels are two independent experiments.

[B] Switching efficiencies for IgG1, IgG2a, IgG2b, and IgG3 were quantified as described above and expressed as a fraction of the efficiency in Aplf$^{+/+}$ cells.

Supplementary Fig. 5

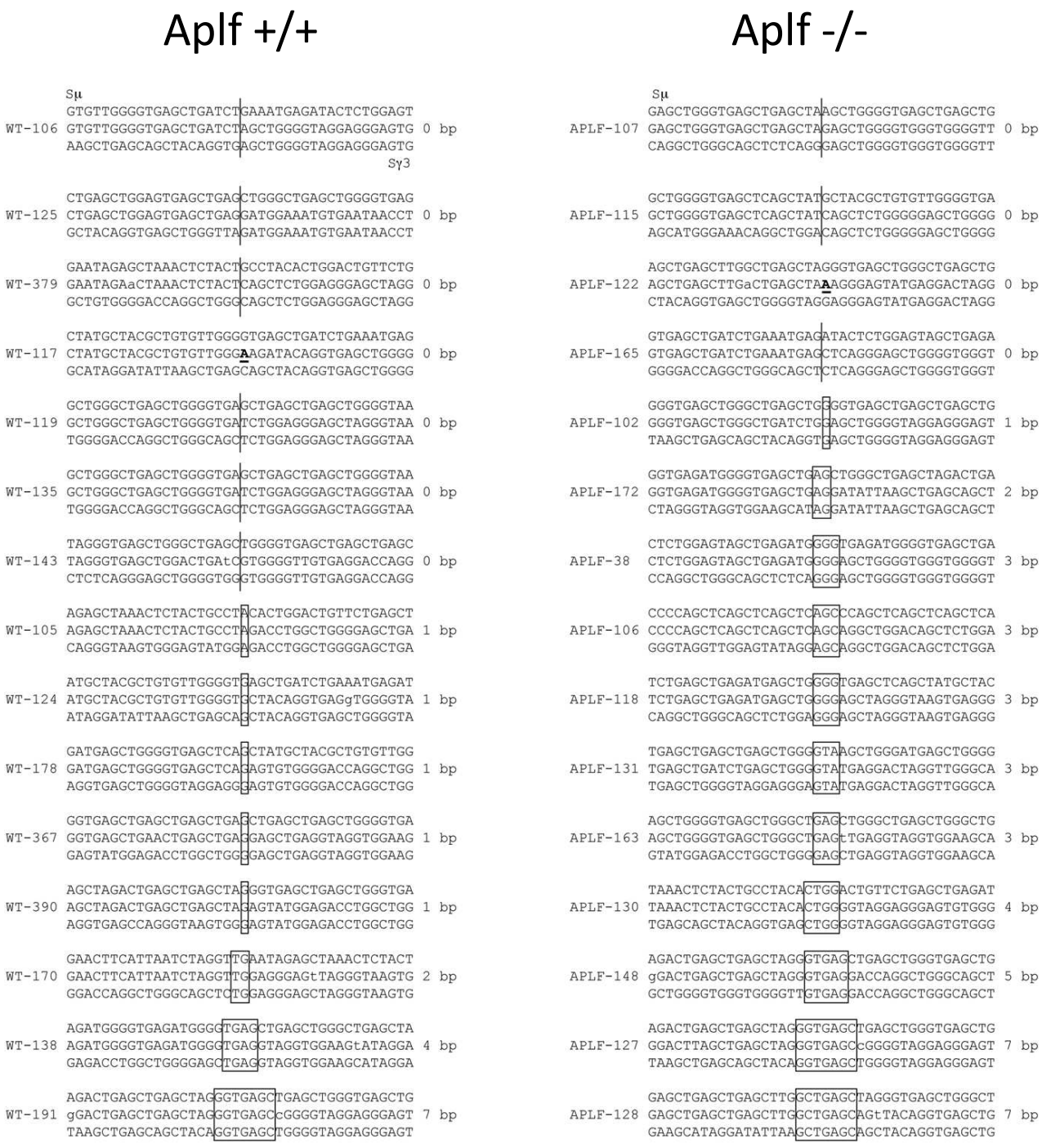

Figure S5: Increased microhomology at CSR junctions in Aplf$^{-/-}$ mouse splenic B cells

[A] Representative Sμ/Sγ3 CSR junctions in Aplf$^{+/+}$ and Aplf$^{-/-}$ splenic B cells. The parental Sμ and Sγ3 sequences (chromosome 12 genomic sequence: NT-114985) are shown above and below the junction sequence, respectively. The region of microhomology at the junction is boxed and

the length of overlap is indicated on the right. Lowercase letters representing mutations and insertions are underlined and in bold.

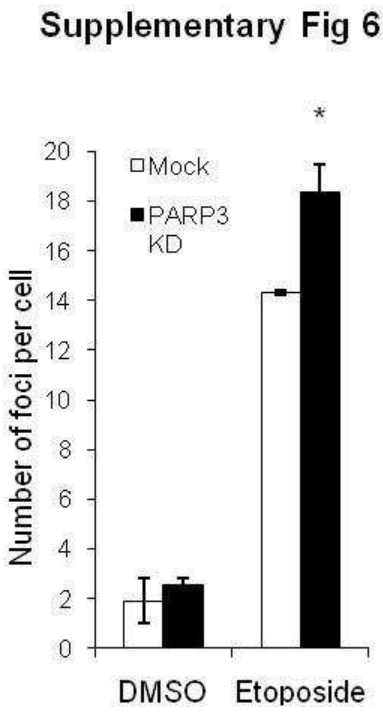

Figure S6: PARP-3 depletion delays the rate of DSBR in Human cells following etoposide
[A] A549 cells mock-depleted (A549) or transiently-depleted of PARP-3 (A549-PARP3^{KD}) were left untreated or incubated with 10μM etoposide for 16 hr, and the average number of γH2AX foci per cell was quantified as described above. Data points are from four replicates, from two independent experiments. Asterisk indicates $p<0.05$ by T-test.

Experimental Procedures

Plasmids and Constructs

pSUPER-APLF, pEYFP-C1-APLF, pEYFP-C1-APLF^{Zfm1}, and pCD2E-His-Myc-APLF were described previously (Iles et al., 2007) as was pCD2E vector (Kadkhodayan et al., 1996), pCI-Puro-His-Myc-APLF (Rulten et al., 2008), pEGFP-XRCC4 (Girard et al., 2004), pSUPER-PARP-1 (Fisher et al., 2007), and pcDNA3.1-Lig4 (Riballo et al., 1999). pcD2E-APLF was generated by subcloning an EcoRI fragment containing the APLF ORF from pEYFP-C1-APLF into pCD2E. pCMV-Tag2A-PARP-3^{TR} was derived from pCMV-Tag2A-PARP-3$_{short}$ (Rouleau et al., 2007) by site-directed mutagenesis (QuikChange; Stratgene) using the oligonucleotides 5'-TCTGGAGCACCTGAGTACAAGGTAATCCAAACCTACTTAGAACAGAC-3' (forward) and 5'- GTCTGTTCTAAGTAGGTTTGGATTACCTTGTACTCAGGTGCTCCAGA-3' (reverse). pSUPER-PARP-3 was generated by annealing complementary 64-mer oligonucleotides (Forward, 5'-GATCCCCGGTGATACAGACCTACTTATTCAAGAGATAAGTAGGTCTGTATCACCTTTTTGGAAA-3') and (Reverse, 5'-AGCTTTTCCAAAAAGGTGATACAGACCTACTTATCTCTTGAATAAGTAGGTCTGTATCACCGGG-3') containing a 19 nucleotide sequence (underlined) from the human PARP-3 ORF and sub-cloning the annealed duplex into pSUPER (OligoEngine)(Brummelkamp et al., 2002). pCMV-Tag2A-PARP3 $^{(H384A, E514A)}$ (PARP3^{TR} CM) was created by site direct mutagenesis from pCMV-Tag2A-PARP-3^{TR} using QuikChange Multi kit (Stratagene) with oligonucleotides 5'-CGGAAGCTGCTGTGGGCTGGCACCAACATGGC-3' and 5'-ACATTCTCCCAGAGCGCGTACCTCATCTACCAG-3'. Cloned products were confirmed by sequencing. These mutations were chosen based on their impact on the activity of PARP-1, with which the PARP-3 catalytic domain is highly conserved (Kleine et al., 2008; Marsischky et al., 1995).

RNA interference

For transient depletion of either PARP-1, PARP-2, PARP-3 or APLF, A549 cells were transiently-co-transfected (Genejuice, Novagen) with a mixture (2:1 molar ratio) of pCD2E (encoding G418 resistance) and the appropriate pSUPER construct or empty pSUPER vector. After 24 hr, cells were placed in media containing 1.5 mg/ml G418 (Invitrogen) for 5 days. Cells were then seeded onto acid-washed coverslips and incubated in media containing G418 for a further 24 hr followed by a further 12 hr in the absence of G418. Coverslips were then immunolabeled for γH2AX foci as described below. For experiments in which APLF and PARP-3 were transiently co-depleted, A549 cells were transiently-transfected as described above but employing pCD2E and mixtures of either pSUPER-APLF and pSUPER-PARP-3 (1:1 molar ratio), pSUPER-APLF and empty pSUPER (1:1 molar ratio), pSUPER-PARP-3 and empty pSUPER (1:1 molar ratio), or pSUPER alone. For complementation of cells transiently-depleted of PARP-3 with targeting-resistant recombinant human PARP-3 (PARP-3^{TR}), PARP-3 catalytic mutant (PARP-3^{TR} CM) or APLF, pCD2E was replaced where appropriate in transient-transfections with pCMV-Tag2a-PARP-3^{TR}, pCMV-Tag2a-PARP-3^{TR} CM or pCD2E-Myc-APLF, respectively.

G418-resistant wild-type A549 cells and A549 cells stably-depleted of APLF (by stable co-transfection with pcD2E and either pSUPER or pSUPER-APLF, respectively) were described previously (Iles et al., 2007). For complementation of these cells with targeting-resistant APLF, these lines were stably-transfected with empty pCI-Puro, pCI-Puro-His-Myc-$APLF^{TR}$, or pCI-Puro-His-Myc-$APLF^{TR\ Zfm1}$ (Rulten et al., 2008) and selected in the presence of 1.5 mg/ml G418 and 1μg/ml puromycin for 2-3 weeks. Drug-resistant single colonies were then expanded, examined by immunoblotting for normal or near-normal levels of APLF protein, and selected clones expanded further and seeded onto glass coverslips for analysis in γH2AX NHEJ assays as described below. For transient complementation with GFP-XRCC4 and DNA ligase IV (Lig4) mock-treated A549 cells and A549 cells depleted of APLF (Iles et al., 2007) or PARP-3 were seeded onto glass coverslips and transiently-transfected with mixtures of either pEGFP and pcDNA3.1, pEGFP-XRCC4 and pcDNA3.1, or pEGFP-XRCC4 and pcDNA3.1-Lig4 at a ratio of 1μg GFP vector:2μg pcDNA3.1. γH2AX assays were carried out 24-hr after transfection on GFP-positive cells as described below.

Immunofluorescence

Coverslips seeded with A549 cells, as described above, were mock treated or irradiated with 2Gy γIR and incubated at 37°C for the times stated. The cells were then rinsed in PBS, fixed (5 min in 4% paraformaldehyde in PBS), permeabilized (0.2% Triton X-100 for 2 min), blocked (5% NFDM for 30 min), and incubated with anti-phospho-H2AX (Ser 139) MAb (clone JBW301, 1/800 in 1% NFDM in PBS; Upstate). Cells were then washed (three times for 5 min each) in PBS containing 0.1% Tween 20 and 0.02% SDS and incubated for 1 h with Alexa Fluor 488 or 555 goat anti-mouse IgG secondary antibody (1/200 dilution in 1% milk-PBS). The cells were then washed (five times for 5 min each) as described above, stained with DAPI (Sigma), mounted in Vectashield (Vector Labs), and scored for γH2AX foci using a Nikon Eclipse 50i microscope. CENP-F (Abcam ab5; 1:300) was used as a marker for G2 cells where stated. For imaging APLF in A549 cells, these were transfected with pEYFP-C1-APLF or pEYFP-C1-APLF^{Zfm1} prior to irradiation. Confocal images were generated using a Zeiss Axiovert equipped with LSM 520 Meta. For labelling γH2AX foci in MEFs, mouse monoclonal anti-phospho-H2AX from Abcam (ab18311) was used (1:300). For analysis of poly (ADP-ribose) synthesis, mock- or PARP3-depleted A549 cells were seeded onto coverslips, incubated in the presence or absence of 500nM Ku-58948 for 30mins, and treated with 10mM H_2O_2 for 10 minutes on ice. After 1 minute recovery at room temperature, the cells were fixed with 4% paraformaldehyde for 5 minutes and then with ice-cold methanol for 10 minutes at -20°C. Cells were then immunolabelled as described above, using mouse α-PAR (Alexis 10H; 1:200, 1hr, RT) and anti-mouse Alexa Fluor 488 secondary antibody. DNA was counterstained with DAPI before mounting in Vectashield (Vector Labs).

Laser microirradiation

A549 cells were seeded onto glass-bottom dishes (MatTek) and transfected with pEGFP-XRCC4. 24-hr after transfection, cells were pre-incubated for 30 min with 10 μg/ml Hoechst dye 33258 at 37°C. GFP-positive cells were then irradiated with a 351-nm UVA laser focused through a 40x/1.2-W objective using a Zeiss Axiovert equipped with LSM 520 Meta. UVA (4.36 J/m^2) was introduced to an area of approximately 12 μm x 0.1 μm. Images were captured at 30 s intervals.

Recombinant proteins

PARP-1 was generated in Sf9 cells using PARP1 baculovirus and purified on a 3-aminobenzamide affinity resin column as described (Giner et al., 1992). Four different preparations of recombinant human PARP-3 protein were employed. Untagged human PARP-3 purified from insect cells was purchased from Alexis (ALX-201-170-C020), GST-tagged PARP-3 purified from insect cells was purchased from Abcam (ab79638), and His-tagged PARP-3 was expressed both in insect cells and E.coli, in-house. For His-PARP-3 from insect cells, PARP-3 cDNA was subcloned from pCMV-Tag2A-PARP-3^{TR} into pFastbac HTc and expressed using a Bac-to-Bac Expression system (Invitrogen). Cell pellets were resuspended in lysis buffer (25 mM Tris-HCl pH7.0, 300 mM NaCl, 0.5% Triton X-100, 1 mM DTT plus Sigma protease inhibitor cocktail) and His-PARP-3 protein purified on nickel-NTA agarose (Qiagen). For His-PARP-3 from in E.coli**,** the bacterial expression construct pNIC28-Bsa4-PARP3 (Lehtio et al., 2009) was kindly provided by Herwig Schüler, Karolinska Institutet, Stockholm, Sweden. pNIC28-Bsa4-PARP3-CM (catalytic mutant) was generated by subcloning a SbfI/XhoI fragment from pCMV-Tag2A-$PARP3^{(H314A,E514A)}$. BL21(DE3) cells were transformed with these constructs and 500 ml cultures grown to OD_{600}=0.6 before induction with 1mM IPTG at 16ºC overnight. Cells were harvested and lysed in 15ml lysis buffer (100mM Tris-HCl pH 7.5, 100mM NaCl,14mM β-mercaptoethanol, 0.5mM EDTA, 0.5mM PMSF) containing Bug-Buster (Novagen) and lysozyme (15,000 U; Sigma). Lysates were incubated at room temperature for 20 min and insoluble material pelled by centrifugation. His-PARP3 and His-PARP3-CM were then purified from the soluble material, in parallel, using Ni-NTA affinity chromatography. Note that somication was avoided during the preparation of His-PARP-3 from E.coli to minimise the formation of DNA fragments that might otherwise co-purify and autoactivate PARP-3.

ADP ribosylation and slot blotting assays

Ribosylation reactions (25 μl) contained 50 mM Tris-HCl pH 8, 2 mM $MgCl_2$, 1% glycerol, 1.5 mM DTT, and the indicated amount of NAD^+ (Sigma), ^{32}P-NAD^+ (NEN), and DNA. Sonicated salmon sperm DNA (2ng/μl), single- or double-stranded oligonucleotide substrate, or pEGFP-C2 plasmid DNA (Clontech) was added as indicated. Recombinant PARP-1 or PARP-3 proteins

were employed at the concentrations indicated. Reactions were incubated at 30°C for 10 minutes before being analysed by SDS acid-PAGE analysis (7.5% in 30 mM phosphoric acid-Tris, pH 6, 0.1% SDS) and quantified by phosphorimaging (GE Healthcare). Slot blotting experiments were conducted essentially as described previously (Rulten et al., 2008). In brief, recombinant His-PARP-3 or histone H1.2 (Alexis) was slot blotted onto nitrocellulose filter and ribosylated or mock-ribosylated by His-PARP-3 in the presence or absence of NAD^+. After extensive washing the filters were incubated or mock-incubated with His-APLF protein probe and bound APLF detected by polyclonal anti-APLF antibody (SK3595). Sequencing gel analysis of trans-ribosylated histone H1.2 was carried out by ribosylating histone H1.2 in 96-wells plates and releasing the product by trypsinisation as described (Rulten et al., 2008).

Aplf$^{-/-}$ mice

Embryonic stem cells derived from 129P2/OlaHsd mice and containing a pGT0Lxf insertion into intron 7 of the mouse Aplf gene (Supplementary Figure 2) were obtained from Bay Genomics (cell line RRF189) and ES cells were microinjected by the Mutant Mouse Regional Resource Centre at UC Davis into C57BL/6J hosts to generate chimeras, which were then crossed with C57BL/6J mice to obtain heterozygotes. Aplf$^{-/-}$ animals and mouse embryonic fibroblasts were generated by interbreeding. Aplf genotypes were confirmed by PCR using the primers I7_F1: 5'-AGGTGGAGACCTCTTAGCAC-3', I7_R1: 5'-CTCTGGAAGCAAGAACAATG-3', bGeo_F: 5'-CAAATGGCGATTACCGTTGA-3' and bGeo_R: 5'-TGCCCAGTCATAGCCGAATA-3'.

Lymphocyte cultures, flow cytometry, and switch junction analysis

Resting B lymphocytes were isolated from 12-week old spleens using CD43 Microbeads (Miltenyi Biotec), labelled with 5 µM CFSE (Invitrogen) for 10 minutes at 37°C, and cultured with 50 µg/ml LPS (Sigma-Aldrich) alone or in combination with 5 ng/ml IL-4 (Peprotech), or 100 ng/ml IFN-γ (Peprotech). For flow cytometry, single cell suspensions were stained with biotin anti-IgG1 (clone A 85.1; BD), biotin anti-IgG3 (clone R40-82, BD), biotin anti-IgG2b (RMG 2B1, BioLegend), biotin anti-IgG2a (clone Igh 1b 5.7, BD) and PE-Streptavidin (Beckman Coulter). Dead cells were excluded from the analysis by staining with 50 nM ToPro-3

(Invitrogen). Data were collected on a FACSCalibur (BD) or LSRII (BD) and analyzed with the FlowJo software (Tree Star, Inc.). Sμ-Sγ3 switch junctions were amplified using previously described primers and conditions (Robert et al., 2009). PCR products were cloned using TOPO-TA cloning kit (Invitrogen) and sequenced using M13 universal primers. Sequence analysis was performed using Sequence Manager II software (DNASTAR).

Subcellular fractionation

Fractionation experiments were carried out essentially as described (Drouet et al., 2005). In brief, A549 cells (~$2x10^6$ per time-point) were trypsinised, re-suspended in medium, and left un-irradiated or γ-irradiated (20 Gy) before allowing to recover at 37ºC for 5-60 minutes. The cells were then pelleted, washed in ice-cold PBS, and resuspended in ice-cold extraction buffer (50mM HEPES, pH 7.5, 150 mM NaCl, 1 mM EDTA, 0.1% Triton X-100, and Sigma mammalian protease inhibitor cocktail and phosphatase inhibitor cocktail I) for 15 min on ice. Following centrifugation (14000 x g for 3 min) the pellet was re-extracted as above and the supernatants from the two extractions pooled to generate an S1 fraction containing soluble cellular protein. The pellet was then resuspended in Triton-free extraction buffer containing 200μg/ml RNAse A for 30 minutes at room temperature and repelleted (14000 x g for 3 min) to obtain an insoluble P2 fraction including chromatin-bound proteins. Aliquots of S1 (5% of total) and P2 fractions (10% of total) were resuspended in 1x SDS-PAGE sample buffer and analysed by western blotting.

Immunoblotting

Western blots were blocked in 5% (w/v) BSA (for α-XRCC4, and α-histone blots) or 5% (w/v) non-fat dried milk (for all other antibodies) for 30 min at RT and incubated with rabbit α-APLF (SK3595; 1:1000 overnight, 4 ºC) (Iles et al., 2007), mouse α-PARP-1 (Serotec MCA1522G; 1:500, 1hr, RT) rabbit α-PARP-2 (Alexis 210-303; 1:3000, overnight, 4 ºC) rabbit α-PARP-3 (Alexis 210-541; 1:1000 overnight, 4 ºC), rabbit α-XRCC4 (Serotec AHP387; 1:2000 overnight, 4 ºC), mouse α-alpha tubulin (Sigma, clone B512; 1:3000, 1hr, RT), mouse α-actin (Clone AC-40 Sigma; 1:5000, 1hr, RT), or mouse α-histone (Chemicon; 1:1000, overnight, 4 ºC) primary antibody. Anti-mouse or anti-rabbit HRP-conjugated secondary antibodies (Dako Cytomation)

were employed at 1:5000 as appropriate for 1 hr at RT and following extensive washes immunoblots were imaged by ECL (GE Healthcare) and autoradiography.

Figure Legends

Figure 1: PARP-3 depletion delays the rate of DSBR in human cells following γ-irradiation.

[A] Mock-depleted (A549) or transiently-PARP-3-depleted (A549-PARP3^{KD}) A549 cells were pre-treated where indicated with 500 nM PARP inhibitor KU-58948 (+ Pi) and either mock-irradiated ('Unt') or γ-irradiated (2 Gy). Cells were fixed at the times indicated for analysis by γH2AX immunofluorescence. The average number of γH2AX foci per cell is shown. For each of the panels "KD" denotes shRNA-mediated knock-down.

[B] A549 cells mock-depleted (A549) or transiently-depleted of PARP-1 (A549-PARP1^{KD}) were mock-irradiated ('Unt') or γ-irradiated (2 Gy) and analysed as described above.

[C] Mock-depleted (A549) or transient PARP-2-depleted (A549-PARP2^{KD}) or PARP-3-depleted (A549-PARP3^{KD}) A549 cells were mock-irradiated ('Unt') or γ-irradiated (2 Gy) and analysed as described above.

[D] Mock-depleted (A549) or transient PARP-3-depleted (A549-PARP3^{KD}) A549 cells were co-transfected with empty vector (+Vector) or with an expression construct encoding targeting-resistant PARP-3 (+PARP3^{TR}). Mock-irradiated ('Unt') or γ-irradiated (2 Gy) cells were analysed as described above.

[E] Mock-depleted (A549) or transiently-PARP-3-depleted (A549-PARP3^{KD}) A549 cells were co-transfected with either empty vector (+Vector) or with an expression construct encoding either targeting-resistant wild-type PARP-3 (+PARP3^{TR}) or a catalytic-mutant of targeting-resistant PARP-3 (+PARP3^{TR} CM). Mock-irradiated ('Unt') or γ-irradiated (2 Gy) cells were analysed as described above.

[F] Representative western blots showing levels of the indicated proteins in the cells employed in panels A-E, above. Top, levels of PARP-3 ('P3'), PARP-1 (P1), PARP-2 (P2), and tubulin ('tub' in the PARP-3-depleted cells (A549-PARP3^{KD}). Asterisk denotes a non-specific band. Bottom Left, PARP-1, PARP-2 and actin levels in mock-depleted A549 cells (A549), PARP-1-depleted cells (A549-PARP1^{KD}), and PARP-2-depleted cells (A549-PARP2^{KD}). Bottom right, levels of PARP-3 ('P3', arrow) and Tubulin ('tub') in PARP-3-deleted cells (PARP3^{KD})

transfected with either empty vector ('Vect'), expression construct encoding targeting-resistant wild-type PARP-3 (+PARP3^{TR}; 'P3'), or catalytically-mutated targeting-resistant PARP-3 (+PARP3^{TR} CM; 'P3^{CM}').

For each of the above panels "KD" denotes shRNA-mediated knock-down and data are the mean of at least three independent experiments (+/- SEM). p values in parentheses reflect the statistical comparison (2-way ANOVA) between the wild-type (A549) data set and the indicated data set, except for those indicated by a right brace, which reflect the statistical comparison between the indicated data sets. "NS" denotes not significant (p value >0.05). For panel E, p values are from a 2-tailed paired T-test.

Figure 2: PARP-3 activity is stimulated by DSBs in vitro.

[A] Coomassie blue-stained SDS-PAGE gels containing 2.5μg of PARP-3 protein (Alexis, left) or His-PARP-3 (right) employed in these experiments, along with the relevant molecular mass marker (M).

[B] Recombinant human PARP-3 (180nM; Alexis) was incubated with 0.5μM ^{32}P-NAD$^+$/2μM NAD$^+$ in the absence of DNA (-) or in the presence of either 50 ng sonicated salmon sperm DNA (SS) or 2μM of the indicated 30-bp or 43-bp single- or double-stranded oligonucleotide substrates. The single-stranded oligonucleotides were 43F (lane 3), 43R (lane 4), 30F (lane 5), and 30R (lane 6). The double-stranded oligonucleotides were 30F+43R (lane 7; duplex with 13-bp 5'-overhang), 43F+30R (lane 8; duplex with 13-bp 3'-overhang), and 43F+43R (lane 9; duplex with blunt-ends). Reaction products were separated on acid SDS-PAGE gels and analysed by phosphorimaging.

[C] Top, pEGFP-C2 plasmid that was either supercoiled (lane 2), linearized with NheI (lane 3; 4-bp 5'-overhang), KpnI (lane 3; 4-bp 3'-overhang), or Eco47III (lane 5; blunt end), or cut at 24 sites per molecule with either Sau3AI (lane 6; 4-bp 5'-overhang) or HhaI (lane 7; 2-bp 3'-overhang), was separated and detected with ethidium bromide/UV following agarose gel electrophoresis. **Middle**, Recombinant human PARP-3 (125nM; Alexis) was incubated with 0.25μM ^{32}P-NAD$^+$/1μM NAD$^+$ as indicated in the absence of DNA or in the presence of 100ng of the indicated pEGFP-C2 plasmid described above. Values below the gel are fold-increases in ribosylated PARP-3 quantified by densitometry and normalised to the band intensity in the

absence of DNA (set at 1), from three independent experiments (+/- SEM in parentheses). **Bottom,** Recombinant human His-PARP-3 (250nM) was incubated with 0.25μM ^{32}P-NAD$^+$/1μM NAD$^+$ and 100ng of the indicated pEGFP-C2 plasmid as described above. Note that in these experiments the concentration of plasmid DSB termini was 0nM (supercoiled), 2.6nM (linear), and 61.4nM (cut x 24).

[D] Left, recombinant human His-PARP-3 (His-P3; 1μM) or GST-PARP-3 (GST-P3; Abcam; 200nM) was incubated with 0.5μM ^{32}P-NAD$^+$/2μM NAD$^+$ as indicated in the absence of 400ng (0.67μM) of an oligonucleotide duplex (30F+43R) with a 13-bp 5'-overhang. Reaction products were separated on acid SDS-PAGE gels, fixed, dried, and detected on a phosphorimager. Right, 2.5μg each of His-PARP-3 (His-P3) or GST-PARP-3 (GST-P3) was fractionated by SDS-PAGE along with molecular mass markers (M) and stained with coomassie blue.

[E] Recombinant wild-type (His-P3) or catalytic mutant (His-P3^{CM}) human His-PARP3 (250nM) purified from E.Coli was incubated with 0.5μM ^{32}P-NAD$^+$/80μM NAD$^+$ in the absence or presence of oligonucleotide duplex DSB substrate (400nM) as indicated. Reaction products were separated on an SDS-PAGE gel, stained with coomassie blue (top), and analysed by phosphorimaging (bottom). The position of His-PARP-3 and His-PARP-3 is shown (P3/ P3^{CM}).

Figure 3: APLF binds PARP-3-ribosylated substrates and accumulates at DSBs in a PARP-activity dependent manner

[A] A549 cells transiently-transfected with pEYFP-APLF (green) were mock-irradiated (-IR, top) or γ-irradiated (2Gy) (+IR, bottom) and 30 min later fixed and immunostained with anti-γH2AX antibody (red). DNA was counterstained with DAPI (blue).

[B] A549 cells transiently-transfected with expression construct encoding either pEYFP-APLF or pEYFP- APLF^{Zfm1} (harbouring a mutated ADP-ribose-binding PBZ domain) were analysed as described above and the fraction of transfected (green) cells with detectable YFP foci was quantified. Where indicated, cells were pre-treated with the PARP inhibitor KU-58948 (500nM) for 30 min prior to γ-irradiation (+Pi).

[C] Top Left, His-PARP-3 and histone H1 (1.9μM each) were incubated separately or together in the presence of 0.25μM ^{32}P-NAD$^+$ in ribosylation buffer containing 50ng DNA for 10 min at

30°C. Reactions products were separated by SDS-PAGE and analysed by phosphorimager. A coomassie stained gel of the recombinant His-PARP-3 and histone H1.2 employed above is shown. Bottom Left, 1μg of either histone H1.2 (H1.2) or 0.5μg His-PARP-3 (His-P3) was slot blotted onto nitrocellulose and either stained with amido black as a loading control (right panel) or incubated with His-PARP-3 (3μM) in the presence or absence of 150μM NAD^+ (+/-NAD) as indicated (left panel). The filters from mock-ribosylation (-NAD) and ribosylation (+NAD) reactions were then incubated or not with APLF probe (10nM), as indicated. After extensive washes bound APLF was detected with anti-APLF antibody. Right, multiwell dishes coated with histone H1.2 were incubated with 1.5μM BSA or His-PARP-3 in the presence of 2μM ^{32}P-NAD^+ and 600ng (24ng/μl) Sau3AI-cut pEGFP-C2 plasmid and after extensive washing reaction products were released from the multiwell dishes by trypsin digestion, fractionated on a polyacrylamide sequencing gel, and detected by phosphorimager. The position of mADPR (n) and pADPR of two or more units (2n, 3n, 4n etc) are indicated.

Figure 4: PARP-3 and APLF function cooperatively during DSBR

[A] A549 cells mock-depleted (A549) or transiently-depleted of either PARP-3 (A549-$PARP3^{KD}$) or APLF (A549-$APLF^{KD}$), or of both PARP-3 and APLF (A549-$PARP3^{KD}$/A549-$APLF^{KD}$), were γ-irradiated (2 Gy). Cells were harvested at the indicated times following irradiation and the average number of γH2AX foci per cell was quantified. Right, Western blot showing APLF, PARP-3, and Actin protein levels in the cells employed above.

[B] A549 cells mock-depleted (A549) or transiently-depleted of APLF (A549-$APLF^{KD}$) were mock-treated or treated with the PARP inhibitor (PARPi) KU-58948 (500nM) for 30 min as indicated prior to mock-irradiation or γ-irradiation (2 Gy). Cells were harvested at the indicated times following irradiation and the average number of γH2AX foci per cell was quantified.

[C] A549 cells mock-depleted (A549) or transiently-depleted of PARP-1 (A549-$PARP1^{KD}$) or both APLF and PARP-1 (A549-$PARP1^{KD}$/$APLF^{KD}$) were mock-treated or treated with the PARP inhibitor KU-58948 (500nM) for 30 min as indicated (+/-PARPi) prior to mock-irradiation or γ-

irradiation (2 Gy). Cells were harvested at the indicated times following irradiation and the average number of γH2AX foci per cell was quantified.

For each of the above panels "KD" denotes shRNA-mediated knock-down and data are the mean of three independent experiments (+/-sem). p values in parentheses reflect the statistical comparison (2-way ANOVA) between the wild-type (A549) data set and the indicated data set, except for those indicated by a right brace, which reflect the statistical comparison between the indicated data sets. "NS" denotes not significant (p value >0.05). Note that the data in Panels B and C of this figure, and also panel B of Figure 1, are from the same experimental set (i.e. were conducted together) but are presented separately for clarity. The "A549" control and "A549-PARP1^{KD}" data sets, where duplicated in these panels, are thus the same.

Figure 5: APLF over-expression restores rapid rates of DSBR in PARP-3 depleted cells

[A] A549 cells mock-depleted (A549) or stably-depleted of APLF (A549-APLF^{KD}) were stably-transfected with empty pCI-Puro vector (A549 APLF^{KD} + Vector) or pCI-Puro-construct encoding targeting resistant APLF (A549 APLF^{KD} + APLF^{TR}) or APLF^{Zfm1} harbouring a mutated ADP-ribose binding PBZ domain (A549 APLF^{KD} + APLF Zfm1^{TR}). Cells were mock-irradiated of γ-irradiated (2 Gy), harvested at the indicated times following irradiation and the average number of γH2AX foci per cell quantified. The bottom panels are Western blots showing APLF levels in the cell lines employed above. An actin blot is included as a loading control.

[B] A549 cells mock-depleted (A549, A549+APLF) or transiently-depleted (A549-PARP3^{KD}, A549- PARP3^{KD} +APLF) of PARP-3 and either mock-complemented (A549, A549-PARP3^{KD}) or complemented (A549+APLF, A549- PARP3^{KD} +APLF) with recombinant human APLF were analysed as described above. The bottom panels are Western blots showing APLF levels in the cell lines employed above. An actin blot is included as a loading control.

For each of the above panels "KD" denotes shRNA-mediated knock-down and data are the mean of three independent experiments (+/-sem). p values in parentheses reflect the statistical comparison (2-way ANOVA) between the wild-type (A549) data set and the indicated data set, except for those indicated by a right brace, which reflect the statistical comparison between the indicated data sets. "NS" denotes not significant (p value >0.05).

Figure 6: APLF promotes XRCC4 retention in damaged chromatin

[A] A549 cells mock-depleted (A549) or stably-depleted of APLF (A549-APLF^{KD}) were transiently-transfected with pEGFP-XRCC4 (green). 24 hr after transfection, transfected cells were locally irradiated with a UVA laser and pEGFP-XRCC4 accumulation at the site of damage quantified for the indicated period (seconds). Data are plotted as the percentage increase in fluorescence (arbitrary units) at the site of UVA irradiation, following irradiation. Data are the mean of >50 cells. Right panel, a representative example of mock-depleted and APLF-depleted cells before and after UVA irradiation.

[B] A549 cells stably-depleted of APLF (A549-APLF^{KD}) and either mock-complemented (A549-APLF^{KD}/Vector) or complemented with targeting-resistant APLF (A549-APLF^{KD}/APLF^{TR}) or targeting-resistant APLF Zfm1 (A549-APLF^{KD}/APLF^{TR}) were transiently-transfected with pEGFP-XRCC4 and analysed as described above.

[C] A549 cells mock-depleted (A549) or stably-depleted of APLF (A549-APLF^{KD}) were mock-irradiated or γ-irradiated (20 Gy) and then fractionated at the times indicated into soluble cellular (S1) and insoluble/chromatin-bound (P2) protein. Aliquots of each fraction were separated by SDS-PAGE and immunoblotted for the proteins indicated.

Figure 7: The DSBR defect in APLF-depleted and PARP-3-depleted cells is complemented by XRCC4/Lig4 over-expression and impacts on class switch recombination.

[A] A549 cells mock-depleted (WT) or stably-depleted of APLF (APLF KD) were transiently-transfected with expression constructs encoding GFP, GFP-XRCC4, or Lig4 singly or in combination, as indicated. Cells were mock-irradiated or γ-irradiated (2 Gy) 24 hr after transfection and the average number of γH2AX foci/per cell quantified at the indicated times following irradiation. “KD” denotes APLF knockdown and data are the mean of three independent experiments (+/-sem). p values in parentheses reflect the statistical comparison (2-way ANOVA) between the wild-type (WT + GFP) data set and the indicated data set, except for those indicated by a right brace, which reflect the statistical comparison between the indicated data sets. “NS” denotes not significant (p value >0.05).

[B] Mock-depleted (WT) or transient-PARP-3-depleted (PARP-3 KD) A549 cells were transiently-transfected with expression constructs encoding GFP or GFP-XRCC4 and Lig4 in combination, as indicated. Cells were mock-irradiated or γ-irradiated (2 Gy) 24 hr after transfection and the average number of γH2AX foci/per cell quantified at the indicated times following irradiation, as described above.

[C] Primary MEFs derived from $Aplf^{+/+}$ ('WT'), $Aplf^{+/-}$ ('HT'), and $Aplf^{-/-}$ ('KO') mouse embryos were mock-irradiated or γ-irradiated (2 Gy) 24 hr after transfection and the average number of γH2AX foci/per cell quantified at the indicated times following irradiation. Data are the mean of three independent experiments (+/-sem) and p values in parentheses reflect the statistical comparison (2-way ANOVA) between the wild-type (WT) data set and the indicated data set. "NS" denotes not significant (p value >0.05).

[D] Sμ/Sγ3 switch regions in genomic DNA from cultured $Aplf^{+/+}$ and $Aplf^{-/-}$ splenic mouse B lymphocytes were PCR amplified, cloned, and sequenced. Histograms represent the percentage of Sμ/ Sγ3 class switch junctions with the indicated length of microhomology. The mean length (bp) of microhomology (MH) and the number of sequences analyzed (n) are indicated. Sequences with small insertions (1-3 nucleotides) at the junction were scored as zero microhomology and are shown in white. The difference in mean length of microhomology between $Aplf^{+/+}$ and $Aplf^{-/-}$ class switch junctions was confirmed as statistically significant by Mann-Whitney (p=0.035).

[E] Model for PARP-3/APLF Acceleration of NHEJ. PARP-3 is activated at a DSB and autoribosylates itself and trans-ribosylates histone H1 (Top). This event may occur before or after DNA-PK dependent events. APLF is then recruited to DSBs via binding of its PBZ domain to ribosylated histone H1 (middle). APLF renders chromatin surrounding the break more 'permissive' for DNA ligation, thereby accelerating DNA ligation (bottom). APLF may render chromatin more 'permissive' by stabilising of XRCC4/Lig4 binding/retention at the break via direct interaction and/or may modify chromatin structure directly. Yellow ovals with blue lines denote nucleosomes and DNA, respectively, and blue ovals denote histone H1. Red lines denote mADPr and/or pADPr.

Figure S1: γ-ray induced γH2AX foci and PARP-3 Activity.

[A] Representative images of untreated A549 cells (left) or A549 cells 30 min after 2Gy γ-radiation (right), immunostained for γH2AX (green) and counterstained with DAPI (blue).

[B] Inhibition of PARP-3 by KU-58948 in vitro. 125nM PARP-3 was incubated with 80μM NAD^+, 250nM ^{32}P-NAD^+, and 100ng pEGFP-C2 plasmid cut at 24 sites per molecule with Sau3AI. Reaction products were analysed by SDS acid-PAGE and autoradiaography.

[C] Mock-depleted (A549) or stably APLF-depleted (A549-$APLF^{KD}$) A549 cells were left untreated or were γ-irradiated (2Gy, left panel; 1Gy, right panel). The average number of γH2AX foci per cell was quantified in untreated cells (Unt) and in γ-irradiated cells harvested at the indicated times following irradiation in CENPF-negative cells (G1) and CENPF-positive cells (G2).

[D] Representative images of mock-depleted or PARP-3-depleted A549 cells 1 min after treatment with 10mM H_2O_2 to induce PARP-1 and PARP-2 dependent pADPr synthesis. Cells were pre-incubated or not, as indicated, with 500nM KU-58948 for 30 min prior to treatment. pADPr was detected with anti-pADPr antibody 10H (green) and DNA was counterstained with DAPI (blue).

Figure S2: PARP-3 is stimulated by DSBs

[A] The indicated amount of recombinant human PARP-3 (Alexis) was incubated with 0.5μM ^{32}P-NAD^+/2μM NAD^+ in the presence of 50 ng sonicated salmon sperm DNA and in the presence or absence of 1nM PARP-1 as indicated. Reaction products were analysed as described in Fig.2.

Figure S3: Generation of $Aplf^{-/-}$ mice

[A] Schematic representation of the gene-trap pGT0Lxf insertion into intron 7 of the mouse Aplf chromosomal sequence. Primers used for genotyping are shown: I7_F and I7_R span the insertion site and were used to detect the wild-type Aplf allele, whereas bGeo_F and bGeo_R were used to detect insertion of the bGeo cassette in the disrupted allele. En2Intr1 = 1.5 kb of

Mouse En2 intron 1; SA = splice acceptor site; Lox71, LoxP and FRT sites enable reversion of the gene-trap using Cre or Flp recombinase.

[B] Predicted Aplf protein structure resulting from wild-type (WT) and knockout (KO) alleles.

[C] Representative genotyping result for $Aplf^{+/+}$, $Aplf^{+/-}$, and $Aplf^{-/-}$ using I7_F and I7_R (lanes 1, 3 and 5) or bGeo_F and bGeo_R (lanes 2, 4 and 6) primers.

Figure S4: Normal frequencies of class switch recombination in $Aplf^{-/-}$ mouse splenic B cells.

[A] FACS analysis for IgG1 cell surface expression in $Aplf^{+/+}$, $Aplf^{+/-}$, and $Aplf^{-/-}$ splenic B lymphocytes stimulated with LPS + IL-4. The percentage of IgG1+ cells is indicated in each plot. Cell division was measured by CFSE dye dilution. Top and bottom panels are two independent experiments.
[B] Switching efficiencies for IgG1, IgG2a, IgG2b, and IgG3 were quantified as described above and expressed as a fraction of the efficiency in $Aplf^{+/+}$ cells.

Figure S5: Increased microhomology at CSR junctions in $Aplf^{-/-}$ mouse splenic B cells

[A] Representative Sμ/Sγ3 CSR junctions in $Aplf^{+/+}$ and $Aplf^{-/-}$ splenic B cells. The parental Sμ and Sγ3 sequences (chromosome 12 genomic sequence: NT-114985) are shown above and below the junction sequence, respectively. The region of microhomology at the junction is boxed and the length of overlap is indicated on the right. Lowercase letters representing mutations and insertions are underlined and in bold.

Figure S6: PARP-3 depletion delays the rate of DSBR in Human cells following etoposide

[A] A549 cells mock-depleted (A549) or transiently-depleted of PARP-3 (A549-$PARP3^{KD}$) were left untreated or incubated with 10μM etoposide for 16 hr, and the average number of γH2AX foci per cell was quantified as described above. Data points are from four replicates, from two independent experiments. Asterisk indicates $p<0.05$ by T-test.

References

Brummelkamp, T.R., Bernards, R., and Agami, R. (2002). A system for stable expression of short interfering RNAs in mammalian cells. Science 296, 550-553.

Drouet, J., Delteil, C., Lefrancois, J., Concannon, P., Salles, B., and Calsou, P. (2005). DNA-dependent protein kinase and XRCC4-DNA ligase IV mobilization in the cell in response to DNA double strand breaks. J Biol Chem 280, 7060-7069.

Giner, H., Simonin, F., de Murcia, G., and Menissier-de Murcia, J. (1992). Overproduction and large-scale purification of the human poly(ADP-ribose) polymerase using a baculovirus expression system. Gene 114, 279-283.

Girard, P.M., Kysela, B., Harer, C.J., Doherty, A.J., and Jeggo, P.A. (2004). Analysis of DNA ligase IV mutations found in LIG4 syndrome patients: the impact of two linked polymorphisms. Hum Mol Genet 13, 2369-2376.

Iles, N., Rulten, S., El-Khamisy, S.F., and Caldecott, K.W. (2007). APLF (C2orf13) is a novel human protein involved in the cellular response to chromosomal DNA strand breaks. Mol Cell Biol 27, 3793-3803.

Kadkhodayan, S., Salazar, E.P., Lamerdin, J.E., and Weber, C.A. (1996). Construction of a functional cDNA clone of the hamster ERCC2 DNA repair and transcription gene. Somat Cell Mol Genet 22, 453-460.

Kleine, H., Poreba, E., Lesniewicz, K., Hassa, P.O., Hottiger, M.O., Litchfield, D.W., Shilton, B.H., and Luscher, B. (2008). Substrate-assisted catalysis by PARP10 limits its activity to mono-ADP-ribosylation. Mol Cell 32, 57-69.

Lehtio, L., Jemth, A.S., Collins, R., Loseva, O., Johansson, A., Markova, N., Hammarstrom, M., Flores, A., Holmberg-Schiavone, L., Weigelt, J., et al. (2009). Structural basis for inhibitor specificity in human poly(ADP-ribose) polymerase-3. J Med Chem 52, 3108-3111.

Marsischky, G.T., Wilson, B.A., and Collier, R.J. (1995). Role of glutamic acid 988 of human poly-ADP-ribose polymerase in polymer formation. Evidence for active site similarities to the ADP-ribosylating toxins. J Biol Chem 270, 3247-3254.

Riballo, E., Critchlow, S.E., Teo, S.H., Doherty, A.J., Priestley, A., Broughton, B., Kysela, B., Beamish, H., Plowman, N., Arlett, C.F., et al. (1999). Identification of a defect in DNA ligase IV in a radiosensitive leukaemia patient. Curr Biol 9, 699-702.

Robert, I., Dantzer, F., and Reina-San-Martin, B. (2009). Parp1 facilitates alternative NHEJ, whereas Parp2 suppresses IgH/c-myc translocations during immunoglobulin class switch recombination. J Exp Med 206, 1047-1056.

Rouleau, M., McDonald, D., Gagne, P., Ouellet, M.E., Droit, A., Hunter, J.M., Dutertre, S., Prigent, C., Hendzel, M.J., and Poirier, G.G. (2007). PARP-3 associates with polycomb

group bodies and with components of the DNA damage repair machinery. J Cell Biochem 100, 385-401.

Rulten, S.L., Cortes-Ledesma, F., Guo, L., Iles, N.J., and Caldecott, K.W. (2008). APLF (C2orf13) is a novel component of poly(ADP-ribose) signaling in mammalian cells. Mol Cell Biol 28, 4620-4628.